Chapter 7. Dynamic Polarization Potential

Contents

1 Introduction **186**

2 Dynamic polarization potential **186**
2.1 Construction of DPP 186
2.2 Dispersion relations 188
2.3 Coulomb excitation effects 189

3 Elastic scattering, direct reaction, and fusion **190**
3.1 Decomposition of DPP into DR and fusion parts 190
3.2 Elastic, direct reaction, and fusion cross sections 191
3.3 A phenomenological analysis with a local DPP 193

4 Localization of the nonlocal DPP **196**
4.1 Methods for Localization 196
4.1.1 Trivially equivalent local potential 196
4.1.2 Taylor expansion method 197
4.1.3 Fourier transformation method 197
4.1.4 Comparisons in the Perey-Buck nonlocal potential 197
4.2 Localized W_F and W_D 198
4.3 Comparison of a localized DPP with the phenomenological OM potential 198

5 Summary **198**

This chapter is a part of the papers by B. T. Kim, entitled "Dynamic polarization potential" in *Proceedings of the third symposium on "Selected topics in nuclear physics"*, Seoul, Hanlimwon, (1990), edited by D. P. Min, and B. T. Kim and T. Udagawa, entitled "Dynamical fusion and direct reaction polarization potentials for heavy-ion scattering and fusion at sub-Coulomb-barrier energies.", Phys. Lett. B **273**, 37-41 (1991).

1 Introduction

The major goal of low-energy nuclear reaction theory is to describe all the different types of nuclear reactions based on a *single* unified approach. Reactions between two nuclei are generally characterized by the impact parameters. For a large impact parameter the elastic scattering is dominant and is well described by the optical model. Inelastic scattering and few-nucleon transfer reactions occur in the grazing collision. Here the multi-step direct reaction theories, like the distorted wave Born approximation, coupled-channels Born approximation, coupled-reaction channels and so on, have explained nicely the observed peripheral phenomena. In the almost head-on collisions, a thorough amalgamation of the two-colliding systems, usually referred to as fusion, is a dominant process. An approach has been suggested [1,2] to interpret the general behavior of fusion based on the coupled-channels(CC) direct reaction theories[3], in which fusion is proceeded through the formation of a compound nucleus.
With this CC formalism, one could explain, in principle, the low energy reaction phenomena on the same footing[4,5]. In fact, such attempts have recently been made in a limited coupling scheme to the low lying excited states for several systems, and explained reasonably well the observed elastic scattering, inelastic scattering, few nucleon transfer reactions, and fusion data. However, the calculations are quite involved when the dimension of the CC equations becomes larger. In addition to this, there are some other difficulties. The CC potential associated with the CC space is not well known. All coupling information, mostly unknown for most of nuclei, should be input to the calculation. Studies concerning the reduction to a one-channel description have thus attracted interest. The dynamical polarization potential (DPP), which describes the effects of coupling to the non-elastic channels, represents the potential for such a one-channel formalism.
In this lecture, we describe the formal background of the DPP following the projection operator method of Feshbach[6], and dispersion relations in Sec. 2. We present a method to calculate the elastic scattering, direct reaction, and fusion cross sections in a model with the DPP in Sec. 3. A method to solve the nonlocal Schrödinger equations is introduced, and the separation of the DPP into fusion and direct reaction (DR) parts is formulated. As an example, we present a phenomenological analysis of elastic scattering, direct reactions, and fusion data for the ^{16}O+^{208}Pb system near the Coulomb barrier energy. Sec. 4 is devoted to the nonlocality problem. We present several localization methods and compare a localized DPP with the phenomenological local optical model potential.

2 Dynamic polarization potential

Here we briefly introduce the DPP in the Feshbach formalism. The dispersion relation between the real and imaginary parts of the potential, and its consequences are also mentioned.

2.1 Construction of DPP

The present study is based on the Feshbach formalism[6], where the Schrödinger equation for the Hamiltonian H becomes two coupled equations,

$$(E - \mathcal{H}_{\mathcal{PP}})\mathcal{P}\Psi = \mathcal{H}_{\mathcal{PQ}}\mathcal{Q}\Psi, \quad (1)$$
$$(E - \mathcal{H}_{\mathcal{QQ}})\mathcal{Q}\Psi = \mathcal{H}_{\mathcal{QP}}\mathcal{P}\Psi. \quad (2)$$

Here Ψ is the total wave function of the original Hamiltonian H, and

$$\mathcal{H}_{\mathcal{PP}} = \mathcal{P}H\mathcal{P}, \ \ \mathcal{H}_{\mathcal{PQ}} = \mathcal{P}H\mathcal{Q}. \quad (3)$$

In Eq. (2.3), $\mathcal{P}$ is the projection operator onto the model space spanned by the direct reaction channel states. $\mathcal{Q} = 1$ - $\mathcal{P}$ is the projection operator onto the rest of the space. It includes open DR channels as well as all the closed channels. $\mathcal{H}_{\mathcal{PP}}$ is responsible for reactions leading to the DR channels, while $\mathcal{H}_{\mathcal{PQ}}$ couples $\mathcal{Q}\Psi$ to $\mathcal{P}\Psi$.

By eliminating $\mathcal{Q}\Psi$ in Eqs. (2.1) and (2.2), the effective Hamiltonian is obtained as,

$$H^{eff} = \mathcal{H}_{\mathcal{PP}} + \mathcal{H}_{\mathcal{PQ}}\frac{1}{E - \mathcal{H}_{\mathcal{QQ}} + i\eta}\mathcal{H}_{\mathcal{QP}}. \quad (4)$$

The Hamiltonian H^{eff} given by Eq. (2.4) defines the coupled-channels or coupled-reaction-channel problem. It is easy, for instance, to derive the CC or CRC equations from the Schrödinger equation for H[5]. If we choose $\mathcal{P}\Psi$ as the elastic channel, then H^{eff} satisfies the optical model Schrödinger equation

$$(E - H^{eff})\chi_0^{(+)} = 0, \tag{5}$$

where $\chi_0^{(+)}$ is the optical model distorted wave function. The effective optical model Hamiltonian H^{eff} becomes

$$H^{eff} = \mathcal{H}_{00} + \mathcal{H}_{0\mathcal{Q}}\frac{1}{E - \mathcal{H}_{\mathcal{Q}\mathcal{Q}} + i\eta}\mathcal{H}_{\mathcal{Q}0}. \tag{6}$$

The first term on the right hand side (RHS) of Eq.(2.6) is the sum of a kinetic energy operator and a bare potential which account for the mean field, and can be calculated from the Hartree-Fock formalism. The second term is called the dynamic polarization potential, ("*dynamic*" because it arises from collisions, "*polarization*" because it represents the distortion of the internal states due to the mutual interaction.) which is the subject of this lecture.

The DPP is absorptive and thus complex since $\mathcal{Q}\Psi$ has open channels. The coupling induces a loss of flux in the elastic channel to $\mathcal{Q}\Psi$. Mathematically, the limit of the Green's function

$$\lim_{\eta\to 0}\frac{1}{E - \mathcal{H}_{\mathcal{Q}\mathcal{Q}} + i\eta} = \mathbf{P}(\frac{1}{E - \mathcal{H}_{\mathcal{Q}\mathcal{Q}}}) - i\pi\delta(E - \mathcal{H}_{\mathcal{Q}\mathcal{Q}}), \tag{7}$$

where $\mathbf{P}$ stands for principal value, is complex. Even if there are no open channels in the $\mathcal{Q}$-space, averaging the fluctuations over energy, which are associated with quasi-bound states due to couplings to the bound states of $\mathcal{H}_{\mathcal{Q}\mathcal{Q}}$, gives a complex DPP. This absorption is to be identified with the loss of flux that goes into compound-nucleus formation.
Furthermore the DPP is nonlocal and intrinsically energy-dependent due to the Green's function in Eq. (2.6). Also it becomes ℓ-dependent as can be seen by a partial wave expansion of the Green's function. The energy dependence of the DPP arises not only from the Green's function but also from the dispersion relations between the real and imaginary parts which are described in the next subsection, and also from the localization of the nonlocal potential when the local potential is adopted. (See Sec. 4.1)
We now construct the DPP more explicitly in the partial wave expansion. For simplicity, we take only two channels, one for elastic, and another for an inelastic channel. We further assume that the spins of both projectile and target are zero and the diagonal and non-diagonal (coupling) potentials are spherically symmetric. The CC equations Eqs. (2.1) and (2.2) for a total angular momentum ℓ may then be expressed as

$$(E - H_\ell)|\chi_\ell >= \sum_{\ell'} v_{\ell\ell'}|\omega_{\ell'} >, \tag{8}$$

$$(E - H_{\ell'})|\omega_{\ell'} >= v_{\ell'\ell}|\chi_\ell >, \tag{9}$$

where χ_ℓ and ω_ℓ are the radial partial wave functions in the elastic and inelastic channels, respectively, and $v_{\ell\ell'}$ is the coupling potential. The Hamiltonian H_ℓ is expressed as

$$H_\ell = -\frac{\hbar^2}{2\mu}(\frac{d^2}{dr^2} - \frac{\ell(\ell+1)}{r^2}) + V_{00}(r) + v_{\ell\ell}(r), \tag{10}$$

where $V_{00}(r)$ is the bare potential. The reduced optical model Schrödinger equation may again be obtained by eliminating $\omega_{\ell'}$ in Eqs. (2.8) and (2.9). The resulting equation reads

$$(E - H_\ell)|\chi_\ell >= U_\ell|\chi_\ell >, \tag{11}$$

where the nonlocal DPP, $U_\ell(r, r')$ is given by

$$U_\ell(r, r') =< r|U|r' >= \sum_{\ell'} v_{\ell\ell'}(r)G_{\ell'}(r, r')v_{\ell'\ell}(r'). \tag{12}$$

The partial wave optical model Green's function $G_\ell(r,r')$ in Eq. (2.12) satisfies

$$(E - H_\ell)G_\ell(r,r') = \delta(r-r'). \tag{13}$$

The explicit form of the radial Green's function may then be given as

$$G_\ell(r,r') = \frac{2m}{\hbar^2}\frac{f_\ell(r_<)h_\ell(r_>)}{W}, \tag{14}$$

where $f_\ell(r)$ and $h_\ell(r)$ are the regular and irregular solutions of H_ℓ, respectively, while W is the Wronskian. Therefore the DPP can easily be constructed in this way, once the coupling potentials are given.

As an example, we calculated the nonlocal DPP for the ^{16}O+^{208}Pb system at an incident ^{16}O energy of E_{lab}=80 MeV. We consider coupling of the ground state to the 2.61 MeV 3^-, 3.20 MeV 5^-, and 4.07 MeV 2^+ states in ^{208}Pb, and to the 6.13 MeV 3^- state in ^{16}O. The coupling potential $v_{\ell\ell'}(r)$ is chosen as the collective form factor. The imaginary part of the $\ell = 10$ polarization potential for this system is shown in Fig. 1a. We clearly see that $U_\ell(r,r')$ is highly nonlocal. We will discuss this problem of nonlocality explicitly in Sec. 4.

2.2 Dispersion relations

The dispersion relation follows immediately from Eq. (2.6) if the eigenstates of $\mathcal{H}_{\mathcal{QQ}}$ are given. Let us assume $\mathcal{H}_{\mathcal{QQ}}$ has discrete states ϕ_α with eigenvalues of E_α, and continuum states $\phi(\epsilon,\alpha)$ with eigenvalues of ϵ, where α is introduced to classify all additional quantum numbers. By substituting these states into $\mathcal{H}_{\mathcal{QQ}}$ in Eq. (2.6), we obtain the following dispersion relation,

$$ReH^{eff} \;=\; H_{00} + \sum_\alpha \frac{\mathcal{H}_{0\mathcal{Q}}|\phi_\alpha><\phi_\alpha|\mathcal{H}_{\mathcal{Q}0}}{E-E_\alpha} - \frac{1}{\pi}\mathbf{P}\int d\epsilon \frac{ImH^{eff}}{E-\epsilon}. \tag{15}$$

What it means is that the real and imaginary parts of the DPP are not independent. This relation also holds when the potential is decomposed into partial waves or orthogonal sets. The dispersion relations are connected to *causality*, which means in the scattering theory that the scattered wave cannot leave the target before the incident wave arrives. The Fourier transformation of the Green's function to the time domain should have $G(t-t') = 0$ for $t < t'$.

The elastic scattering data accumulated have shown that the imaginary part of the optical potential diminishes quite rapidly as the incident energy becomes lower than the Coulomb barrier. This can be understood from the fact that fewer reaction channels are open when the beam energy is lower. The origin of this energy dependence is obviously not from the intrinsic Green's functions, nor from nonlocality. Furthermore, when the optical potential at a fixed point around the strong absorption radius is plotted as a function of energy, the real depth of the potential is shown to be a bell shape, peaked around the Coulomb barrier. This is because the coupling of the elastic channel to other reaction channels gives rise to the polarization effect. Recently, Nagarajan et al.[7] suggested a local form of the dispersion relation for the two colliding nuclei as,

$$V(r,E) = V(r,E_s) + \frac{E-E_s}{\pi}\mathbf{P}\int d\epsilon \frac{W(r,\epsilon)}{(\epsilon-E)(\epsilon-E_s)}, \tag{16}$$

where V and W are the real and imaginary parts of optical potential, respectively. The first term of the RHS, $V(r,E_s)$ is the sum of the first and second terms of Eq. (2.15) and E_s is the energy where the normalization is done to give a correct magnitude of the potential depth. They showed that an observed bell-shaped real potential at a fixed point is a consequence of the dispersion relation, when the imaginary part suddenly changes near the Coulomb barrier.

The sudden increase in the real depth of the potential at near-barrier energies allows for a lowering of the barrier, and enhances the penetrability of the incident wave through the barrier. It can account for anomalously large fusion cross sections recently observed in subbarrier heavy-ion fusion reactions. Therefore the dispersion relation plays a crucial role in explaining not only elastic scattering but also fusion near the barrier.

2.3 Coulomb excitation effects

In the late nineteen seventies, people calculated the polarization potential due to the electric 2^λ-pole Coulomb excitation. The simplest expression was given by Love et al. (Phys. Lett., **72B**, 4 (1977)). The real part is negligible, while for a single $E2$ excitation, the absorptive part reduces to

$$\begin{aligned} \Im U_p(r) &= -[1 - \frac{2}{7}(\frac{R_C}{r})^2 - \frac{1}{21}(\frac{R_C}{r})^4]K_C(r)\frac{W_p(E2)}{r^5}, \quad r \geq R_C \\ &= -\frac{2}{3}K_C(r)\frac{W_p(E2)r^4}{R_C^9}, \quad r < R_C \end{aligned}$$

where K_C is a braking factor due to the reduction of kinetic energy in the repulsive Coulomb field,

$$K_C = [1 - (Z_a Z_A e^2/rE_{cm})]^{-1/2}$$

The strength of the potential is proportional to the reduced transition probability $B(E2)\uparrow$ (in $e^2\text{fm}^4$) for the excitation

$$W_p(E2) = 0.01676\frac{\mu Z_p^2}{k}B(E2)\uparrow g_2 \quad (\text{MeV} \quad \text{fm}^5)$$

where g_2 is an adiabaticity correction factor. Because it has a long range, it induces absorption along orbits whose classical distance of closest approach is much greater than the usual strong-absorption radius and whose angular momenta are much larger than the critical peripheral value. Consequently, the elastic scattering cross section is reduced below the Rutherford value at angles forward of the Fresnel shadow region. This is illustrated in Fig. 12.10.

3 Elastic scattering, direct reaction, and fusion

3.1 Decomposition of DPP into DR and fusion parts

We first show that the imaginary part of the DPP can be separated into direct reaction (DR) and fusion parts. Let us denote the imaginary part of $U_\ell(r,r')$ of Eq. (2.11) as $W_\ell(r,r')$, i.e.,

$$W_\ell(r,r') = ImU_\ell(r,r'). \tag{1}$$

$W_\ell(r,r')$ can then be decomposed into fusion and DR parts, $W_{F;\ell}(r,r')$ and $W_{D;\ell}(r,r')$, respectively, as

$$W_\ell(r,r') = W_{F;\ell}(r,r') + W_{D;\ell}(r,r'). \tag{2}$$

We use for this purpose the identity,

$$ImG_\ell = G_\ell^+[ImU_\ell]G_\ell + \Omega_\ell^+[Img_\ell]\Omega_\ell, \tag{3}$$

where g_ℓ is the free Green's function, while Ω_ℓ is the Möller wave operator which generates the distorted wave function upon operating on the plane wave function,

$$\Omega_\ell = 1 + U_\ell G_\ell. \tag{4}$$

Proof of Eq.(3.3)

By neglecting the subscript ℓ, we have

$$\begin{aligned} G &= g + gUG \\ -G^* &= -g^* - G^*U^*g^* \\ \Im G &= \Im g + \frac{1}{2i}(gUG - G^*U^*g^*) \end{aligned}$$

$$\begin{aligned} A &\equiv \frac{1}{2i}(gUG - G^*U^*g^*) \\ &= \frac{1}{2i}(gUG - g^*UG) + \frac{1}{2i}(G^*U^*g - G^*U^*g^*) + \frac{1}{2i}(g^*UG - G^*U^*g) \\ &= (\Im g)UG + G^*U^*(\Im g) + \frac{1}{2i}(G^*UG - G^*U^*G) + \frac{1}{2i}(G^*U^*g^*UG - G^*U^*gUG) \\ &= (\Im g)UG + G^*U^*(\Im g) + G^*(\Im U)G + G^*U^*(\Im g)UG \end{aligned}$$

Thus we finally obtain

$$\begin{aligned} \Im G &= G^*(\Im U)G + (1+G^*U^*)(\Im g)(1+UG) \\ &= G^*(\Im U)G + \Omega^*(\Im g)\Omega \qquad\qquad Q.E.D. \end{aligned}$$

By substituting Eqs. (3.2), (3.3) and (3.4) into Eq. (2.11), $W_{F;\ell}(r,r')$ and $W_{D;\ell}(r,r')$ can be expressed as

$$W_{F;\ell}(r,r') = \sum_{\ell'}[w_{\ell\ell'}G_{\ell'}v_{\ell'\ell} + v^+_{\ell\ell'}G^+_{\ell'}w_{\ell'\ell} + v^+_{\ell\ell'}G^+_{\ell'}W_{\ell'\ell'}G_{\ell'}v_{\ell'\ell}], \tag{5}$$

$$W_{D;\ell}(r,r') = \sum_{\ell'} v^+_{\ell\ell'}\Omega^+_{\ell'}[Img_{\ell'}]\Omega_{\ell'}v_{\ell'\ell}, \tag{6}$$

where $w_{\ell\ell'}$ and $W_{\ell\ell}$ are the imaginary parts of $v_{\ell\ell'}$ and H_ℓ of Eq. (2.10), respectively. The first two terms on the RHS of Eq. (3.5) describes the absorption occurring during transitions, and vanishes when the real coupling form factors are used. The last one represents absorption into the compound nucleus from the elastic and nonelastic channels. $W_{D;\ell}$ of Eq. (3.6) is the part of the imaginary potential that accounts for the direct reaction.

We again calculated the nonlocal $W_{F;\ell}(r,r')$ and $W_{D;\ell}(r,r')$ for the ^{16}O+^{208}Pb system at E_{lab}=80 MeV. The same coupling scheme as the example in Sec. 2.1 was used. The fusion and DR parts of the imaginary potential are displayed in Fig. 1b and 1c. Again they are highly nonlocal. The shape of W in the region of radial distances smaller than the strong absorption radius (about 12.4 fm in this case) is similar to that of W_F, while it looks like W_D in the outer region and decreases rapidly as the radial distance gets larger. This implies that fusion takes place in the inner region and the direct reaction in the nuclear surface region.

3.2 Elastic, direct reaction, and fusion cross sections

The basic optical model equation, Eq. (2.11) becomes a nonlocal integro-differential equation in the r-representation given as

$$(E - H_\ell)\chi_\ell(r) = \int U(r,r')\chi_\ell(r')dr'. \tag{7}$$

Since the celebrated work of Perey and Buck (PB) some 30 years ago[8], little progress has been made in improving the method for solving this equation. PB solved the equation by an iteration method, but convergence depended very critically on the particular local potential $U_0(r)$ used for generating the initial trial solution. The iteration often diverges, even if U_0 differs very slightly from the optimal potential suggested by PB. Because of this, the PB method has not been widely used.

Very recently, Kim and Udagawa [9] presented a new, rapid, and reliable method for solving the nonlocal optical model Schrödinger equation. We briefly explain this method. Henceforth for brevity, we shall write all equations in terms of bra and ket vectors and operators. Eq. (3.7) then becomes

$$(E - H_\ell)|\chi_\ell >= U|\chi_\ell > . \tag{8}$$

Eq. (3.8) can then be transformed into the following integral equation

$$|\chi_\ell >= |\chi_\ell^{(0)} > + G_\ell U|\chi_\ell >, \tag{9}$$

where $|\chi_\ell^{(0)} >$ is the homogeneous solution of Eq. (3.8) with the same outgoing wave boundary condition, and G_ℓ is the Green's function of Eq. (2.14).

Now let us introduce an auxiliary state function $|\lambda_\ell >$ defined as

$$|\lambda_\ell >= U|\chi_\ell >, \tag{10}$$

Multiplying both sides of Eq. (3.9) by U, one obtains an integral equation for $|\lambda_\ell >$,

$$|\lambda_\ell >= |\rho_\ell > + UG_\ell|\lambda_\ell >, \qquad (|\rho_\ell >\equiv U|\chi_\ell^{(0)} >). \tag{11}$$

The above Eq. (3.11) is the equation that we propose to solve. Since both $|\chi_\ell^{(0)} >$ and G_ℓ are defined in terms of the local potential H_ℓ, they can be calculated without any problem. This means that once $|\lambda_\ell >$ is obtained, the optical model wave function $|\chi_\ell >$ can easily be obtained from Eq. (3.9) with the help of Eq. (3.10).

In solving Eq. (3.11), we use the Lanczos method[10]. It is worth noting that the application of the Lanczos method for solving Eq. (3.11) is possible, since $|\lambda_\ell >$ is a bound state vector, as seen from the fact that it is defined by multiplying $|\chi_\ell >$ by a localized operator U. (See Eq. (3.11)). It is thus possible to expand $|\lambda_\ell >$ in terms of an orthonormal set of vectors, as will be seen below in Eq. (3.15). This is not the case for $|\chi_\ell >$ in Eq. (3.9), since $|\chi_\ell >$ is not bounded.

We first expand $|\lambda_\ell >$ in terms of the bi-orthonormal set of vectors $|D_i >$ with *i=0,1,....,N* that are generated according to

$$|D_0 >= \frac{1}{N_0}|\rho_\ell >, \tag{12}$$

$$|D_{i+1}>=\frac{1}{N_{i+1}}[UG_\ell|D_i>-\sum_{j=0}^{i}|D_j>\alpha_{ji}], \tag{13}$$

with

$$\alpha_{ji}=\begin{cases} <\tilde{D}_j|UG_\ell|D_i> & \text{if } j\le i+1 \\ 0 & \text{if } j>i+1. \end{cases} \tag{14}$$

N_i in the above equations is the normalization constant determined from the condition $<\tilde{D}_i|D_i>=1$, $|\tilde{D}_i>$ being the conjugate state to $|D_i>$. The coefficients α_{ji} given by Eq. (3.14) are those determined from the usual Schmidt orthonormalization procedure. We now write $|\lambda_\ell>$ as

$$|\lambda_\ell>=\sum_{i=0}^{N}C_i|D_i>, \tag{15}$$

where C_i are the expansion coefficients. Inserting Eq. (3.15) into Eq. (3.11), one easily derives a set of inhomogeneous linear equations for the expansion coefficients C_i, i.e.,

$$\sum_j(\delta_{ij}-\alpha_{ij})C_j=N_0\delta_{0i}. \tag{16}$$

The values of C_i are then determined by solving Eq. (3.16). Note that Eq. (3.16) can be solved rather easily, because $\alpha_{ji}=0$ for $j>i+1$. In addition, the value of N, i.e., the number of the basic functions D_i, can be chosen as a small number. This greatly helps to make the actual numerical calculations very rapid.

This method was tested for the case of the n+^{208}Pb system with incident energies E_n=7 and 14.5 MeV. The results showed that N=3 was enough to obtain the solution within an accuracy of 0.1%. Note that if one uses the PB method, one needs to do about 10 iterations in order to obtain the solution with the same accuracy. In the case of a highly nonlocal DPP constructed in the previous section, a good agreement with the CC result is achieved with N=8. The larger N-value may be ascribed to the complex nature of nonlocality of the DPP.

Once the optical model wave function is obtained with the method described above, the elastic scattering amplitude can be easily calculated from the outgoing wave boundary condition, and the differential elastic cross section immediately follows.

The total direct reaction and fusion cross sections can be obtained in the following way. The divergence of the current density is given [11] as,

$$div\ \mathbf{j}_\ell=\frac{2}{\hbar}Im(\chi_\ell^{(+)*}(r)U_\ell(r,r')\chi_\ell^{(+)}(r')). \tag{17}$$

The reaction cross section can be obtained by integrating the divergence of the current density all over space and summing over all the partial waves.

$$\sigma_R=\frac{\pi}{k^2}\sum_\ell(2\ell+1)T_{R;\ell}, \tag{18}$$

where the transmission coefficients $T_{R;\ell}$ can be written as

$$T_{R;\ell}=\frac{8}{\hbar v}\int drdr'\chi_\ell^{(+)*}(r)W_\ell(r,r')\chi_\ell^{(+)}(r'). \tag{19}$$

Here v is the relative velocity in the incident channel. If W is decomposed into W_F and W_D, the fusion and direct reaction cross sections, σ_F and σ_D, respectively, can be expressed exactly the same as in Eq. (3.18), but with the corresponding transmission coefficients,

$$T_{F;\ell}=\frac{8}{\hbar v}\int drdr'\chi_\ell^{(+)*}(r)W_{F;\ell}(r,r')\chi_\ell^{(+)}(r'), \tag{20}$$

$$T_{D;\ell}=\frac{8}{\hbar v}\int drdr'\chi_\ell^{(+)*}(r)W_{D;\ell}(r,r')\chi_\ell^{(+)}(r'). \tag{21}$$

Thus all the elastic scattering, direct reaction, fusion cross sections are given in a model with a DPP.

3.3 A phenomenological analysis with a local DPP

We have shown that the DPP can account for all the reaction phenomena if it is properly constructed, including all the nuclear structure information. Unfortunately, it is impossible to make such a construction of the DPP at this stage. In any nuclear reaction calculation, the phenomenological optical model Hamiltonians have thus customarily been used. In the present study, following this usual procedure, we make[12] a simultaneous χ^2-analysis of elastic scattering, DR, and fusion cross sections for the ^{16}O+^{208}Pb system at near- and sub-barrier energies and determine a DPP that satisfies the dispersion relation over all space.

We assume in this analysis the conventional local optical model Hamiltonian,

$$H = H_a + T_a + U_a, \tag{22}$$

satisfying the properties of the DPP we have previously described, namely H satisfies a dispersion relation, and W can be separated into direct reaction and fusion parts. In Eq. (3.15), H_a, T_a and U_a are the intrinsic Hamiltonian, kinetic energy operator for the relative motion between the projectile a and target A, and the so-called optical model potential, respectively. The optical model potential U_a to be used is local, and is given as

$$U_a(r) = U_C(r) - [V_0(r) + V(r) + iW(r)], \tag{23}$$

where $U_C(r)$ is the Coulomb potential and $V_0(r)$ is the bare potential[13,14] that corresponds to the Hartree-Fock potential[15], Note that $V_0(r)$ may have an energy dependence coming from the nonlocality of the exchange contribution. We ignore such effects, however, in the present study, as they are expected to be small for heavy-ion scattering[16]. The quantities V and W in Eq. (3.23) are, respectively, the real and imaginary parts of the DPP originating from couplings to the reaction channels. They are assumed to have a volume-type fusion and surface-derivative-type DR parts. Explicitly, $V_0(r)$, $V(r)$ and $W(r)$ are given, respectively, as

$$\begin{aligned} V_0(r) &= V_0 f(X_0), & (24)\\ V(r) &= V_F(r) + V_D(r) \\ &= V_F f(X_F) + 4V_D a_D \frac{df(X_D)}{dR_D}, & (25)\\ W(r) &= W_F(r) + W_D(r) \\ &= W_F f(X_F) + 4W_D a_D \frac{df(X_D)}{dR_D}, & (26) \end{aligned}$$

where $f(X_i) = [1 + exp(X_i)]^{-1}$ with $X_i = (r - R_i)/a_i$ (i=0,F and D) is the usual Woods-Saxon function.

The optical potential given above involves eleven parameters, excluding the Coulomb radius parameter in U_C, which we fix as $r_c = 1.25$ fm. We have attempted to fix these parameters by a χ^2-analysis. It is, however, impossible to determine all eleven parameters uniquely from a χ^2-analysis; we thus fix *a priori* some of the parameters by taking their values from the literature. Following Refs. 13 and 14, we fixed the parameters of the bare potential $V_0(r)$ as

$$V_0 = 60.4 \text{ MeV}, \quad r_0 = 1.176 \text{ fm}, \quad a_0 = 0.658 \text{ fm}. \tag{27}$$

With these values, $V_0(r)$ has values very similar to those of the folding potential at $r \approx R_A$. Further, we fixed all the geometrical parameters in the local DPP ($V(r) + iW(r)$) as

$$r_F = 1.40 \text{ fm}, \quad a_F = 0.25 \text{ fm}, \tag{28}$$

$$r_D = 1.50 \text{ fm}, \quad a_D = 0.45 \text{ fm}. \tag{29}$$

These values are chosen as the best possible values, taking into consideration results of studies reported in Refs. 13. Note, however, that these values are still not unique, and this non-uniqueness might introduce a certain ambiguity in the present study.

Once the geometrical parameters are fixed in this way, the dispersion relation is reduced to one for the strength parameters V_i and W_i ($i = F$ and D). The relation now reads[7]

$$V_i(E) = V_i(E_s) + \frac{E - E_s}{\pi} \mathbf{P} \int_0^\infty dE' \frac{W_i(E')}{(E' - E_s)(E' - E)}, \tag{30}$$

where $V_i(E_s)$ is the value of the potential at a reference energy $E = E_s$. Using the above relation, it is possible to evaluate values of V_F and V_D, once the values of $W_F(E)$ and $W_D(E)$ are known.

In an attempt to obtain the values of $W_F(E)$ and $W_D(E)$, we first carried out a χ^2-analysis, treating the four strength parameters V_F, V_D, W_F and W_D as adjustable parameters. We took into account all the data[17,18] available for incident energies between E_{lab}=78 MeV and 104 MeV. We included the total DR cross sections, when available, in the χ^2-analysis.

The values of the parameters determined in this way showed, as expected, a considerable fluctuation; i.e., they changed appreciably from one energy point to another, excepting those of W_D. For this exceptional case, the values were determined as a fairly smooth function of E. To illustrate this and also the fluctuation mentioned above, we show in Fig. 2a the values of V_D and W_D. As seen, the V_D-values fluctuate fairly strongly, while those of W_D behave rather smoothly as a function of E. The later W_D-values can be well represented by the following function of E (in units of MeV):

$$W_D(E) = \begin{cases} 0 & \text{for E}\leq 70 \\ 0.0185(E-70) & \text{for } 70<\text{E}\leq 90 \\ 0.37 & \text{for } 90\leq \text{E} \end{cases} \tag{31}$$

The solid line shown in Fig.2a is W_D predicted by the above Eq. (3.31). As seen, the line fits the empirical values rather well.

The fact that W_D could be fixed as a smooth function of E indicates that these values are reliable. There is a reason that W_D can be determined unambiguously, and hence appear as a smooth function of E. The reason lies in the fact that W_D is the dominant absorptive term in the peripheral region. Therefore, the elastic scattering cross section is quite sensitive to the value of W_D. This is not the case for V_D; even in the peripheral region; V_D is generally smaller than the bare potential $V_0(r)$, making it difficult to determine its value unambiguously. The fluctuation seen in Fig. 2a may be understood to arise from this difficulty.

Since a reliable value of W_D is now available, one can generate better values of V_D by using the dispersion relation (3.30). In doing this, we need to know one more parameter, i.e., the value of V_D at $E = E_s$. We may fix this $V_D(E_s)$ by fitting the average of the resultant V_D to that of the empirically determined V_D. The solid curve shown in Fig. 2a shows the V_D-values thus calculated. The $V_D(E_s)$-value used is $V_D(E_s)$=0.5 MeV at E_s=90 MeV. In what follows, we shall use thus calculated $V_D(E)$ as our final $V_D(E)$.

The second χ^2 analysis was then carried out by using the above values for V_D and W_D, and by treating V_F and W_F as adjustable parameters. Fig. 2b shows the values of V_F and W_F thus determined. As seen, both are now determined as fairly smooth functions of E. The W_F-values can now be well represented (in units of MeV) as

$$W_F(E) = \begin{cases} 0 & \text{for E}\leq 77.5 \\ 0.52(E-77.5) & \text{for } 77.5<\text{E}\leq 84 \\ 3.4 & \text{for } 84\leq \text{E}. \end{cases} \tag{32}$$

The solid curve shown in Fig. 2b is the prediction of Eq. (3.32). The curve fits the empirical values reasonably well. We then calculated values of V_F by using Eq. (3.30) and (3.32). The constant value involved was chosen as $V_F(E_s)$=1.8 MeV at E_s=84 MeV. The solid line shown in Fig. 2b is the prediction. As seen, the predicted V_F-values again agree reasonably well with the empirically determined values, except at the lowest energy point (E=78 MeV). The discrepancy seen there, however, should not be taken too seriously, since the data are rather insensitive to

the V_F-values at such a low energy. Except for this point, the empirically determined V_F and W_F are seen to satisfy the dispersion relation fairly well.

This result then suggests that we may use, as our final potential, the one with W_F and W_D given, respectively, by Eqs. (3.32) and (3.31), and also V_F and V_D generated from the dispersion relation as done above. This potential fully satisfies the dispersion relation. It can also nicely reproduce the data. This is seen in Fig. 3, where we have presented $R = \sigma_{EL}/\sigma_{RUTH}$ (where σ_{RUTH} is the Rutherford cross section), σ_F and σ_D, calculated by using our final potential. The results are also compared with the experimental data. As seen, all experimental R, σ_F and σ_D results are well reproduced by the calculations.

As an example, we calculate $V(E)$ obtained from the dispersion relation of the following form of $W(E)$,

$$W(E) = \begin{cases} 0 & \text{for } E \le E_a \\ \frac{W_b}{E_b - E_a}(E - E_a) & \text{for } E_a < E \le E_b \\ W_b & \text{for } E_b \le E. \end{cases} \tag{33}$$

We first calculate the principal value of the integral

$$\begin{aligned} I &\equiv \mathbf{P}\int_0^\infty \frac{W(E')dE'}{(E'-E)(E'-E_s)} \\ &= \frac{W_b}{E_b - E_a}\left(\frac{E-E_a}{E-E_s}\mathbf{P}\int_{E_a}^{E_b}\frac{dE'}{E'-E} - \frac{E-E_s}{E_s-E_a}\mathbf{P}\int_{E_a}^{E_b}\frac{dE'}{E'-E_s}\right) \\ &\quad + W_b\left(\frac{1}{E-E_s}\mathbf{P}\int_{E_b}^{\infty}\frac{dE'}{E'-E} - \frac{1}{E-E_s}\mathbf{P}\int_{E_b}^{\infty}\frac{dE'}{E'-E_s}\right) \\ &= W_b\left\{\frac{E-E_a}{(E-E_s)(E_b-E_a)}[\ln(E_b-E) - \ln(E_a-E)] - \ln(E_b-E)\right\} \\ &\quad - W_b\left\{\frac{E_s-E_a}{(E-E_s)(E_b-E_a)}[\ln(E_b-E_s) - \ln(E_a-E_s)] - \ln(E_b-E_s)\right\} \\ &= -\frac{W_b}{E-E_s}\left[\frac{E-E_a}{E_b-E_a}\ln(E-E_a) - \frac{E-E_b}{E_b-E_a}\ln(E-E_b)\right] \\ &\quad + \frac{W_b}{E-E_s}\left[\frac{E_s-E_a}{E_b-E_a}\ln(E_s-E_a) - \frac{E_s-E_b}{E_b-E_a}\ln(E_s-E_b)\right] \end{aligned}$$

By setting $E_s = E_b$, we have

$$\begin{aligned} V(E) &= V(E_b) - \frac{W_b}{\pi}\left[\frac{E-E_a}{E_b-E_a}\ln(E-E_a) - \frac{E-E_b}{E_b-E_a}\ln(E-E_b) - \ln(E_b-E_a)\right] \\ &= V(E_b) - \frac{W_b}{\pi}\left[\frac{E-E_a}{E_b-E_a}\ln\left|\frac{E-E_a}{E_b-E_a}\right| - \frac{E-E_b}{E_b-E_a}\ln\left|\frac{E-E_a}{E_b-E_a}\right|\right] \end{aligned}$$

4 Localization of the nonlocal DPP

Even though the DPP is formulated to be *nonlocal*, the phenomenological *local* optical potential which satisfies the dispersion relations, and is decomposed into fusion and direct reaction parts is shown to explain the observed low-energy nuclear reaction phenomena; elastic scattering, direct reaction, and fusion. This implies that there always exists an equivalent local potential to the nonlocal DPP, or that the DPP itself is local(or that nonlocality of the DPP is small in reality.). Another implication is that we may understand in a simple potential term where the reaction occurs. For example, if $W_F^{OM}(r)$ is proved to actually represent $W_F^{DPP}(r,r')$, then the place where fusion takes place, which is one of the problems in the heavy-ion fusion reactions, can be known. None of these questions have been clearly answered! The first thing to do in order to answer these questions would be to construct the nonlocal DPP in the large CC space including all coupling information, and to see whether it becomes local or not when the CC space gets larger. However, with regard to the present status in nuclear physics, this is a rather difficult task. Another test would be to find an appropriate localization procedure in which the physics remains the same. In this section, we introduce several known localization procedures, apply them to the localization of the DPP, and discuss the results.

4.1 Methods for Localization

The problem we encounter is to find a $U_\ell^L(r)$ which contains all the same physical properties as that of $U_\ell^N(r,r')$. They are related through nonlocal and local Schrödinger equations as,

$$(E-H_\ell)\chi_\ell^N(r) = \int dr' U_\ell^N(r,r')\chi_\ell^N(r'), \tag{1}$$

$$(E-H_\ell)\chi_\ell^L(r) = U_\ell^L(r,)\chi_\ell^L(r). \tag{2}$$

We introduce several approximation methods here.

4.1.1 Trivially equivalent local potential

Franey and Ellis[19] defined the trivially equivalent local potential(TELP) as

$$U_\ell^L(r) = \frac{1}{\chi_\ell}\int dr' U_\ell^N(r,r')\chi_\ell^N(r'), \tag{3}$$

by setting, in Eqs. (4.1) and (4.2),

$$\chi_\ell^L(r) = \chi_\ell^N(r) = \chi_\ell(r) \tag{4}$$

Because $\chi_\ell^L = \chi_\ell^N$, this potential always guarantees the elastic scattering. Apart from the ℓ-independent phenomenological optical potential, it is ℓ-dependent. Because of χ_ℓ in the denominator, this potential varies rapidly where $|\chi_\ell|$ is small.
This localized local potential has an unphysical contribution; the imaginary part of $U^L(r)$ has a contribution from $ReU^N(r,r')$, i.e.,

$$\begin{aligned} ImU_\ell^L(r) &= \tfrac{1}{|\chi_\ell|^2} Im\int dr'\chi_\ell^*(r)U_\ell^N(r,r')\chi_\ell^N(r') \\ &= \tfrac{1}{|\chi_\ell|^2} Re\int dr'\chi_\ell^*(r)[ImU_\ell^N(r,r')]\chi_\ell^N(r') \\ &+ \tfrac{1}{|\chi_\ell|^2} Im\int dr'\chi_\ell^*(r)[ReU_\ell^N(r,r')]\chi_\ell^N(r'). \end{aligned} \tag{5}$$

A similar contribution in $ReU^L(r)$ comes from $ImU^N(r,r')$. This unphysical term is quite significant, and plays an important role in constructing the distorted waves in the elastic channel, and thus in accounting for the elastic scattering when nonlocality becomes large. Of course, it does not affect the direct reaction and fusion cross sections, since the integration of this term over all space vanishes. Fig. 4 displays each term in Eq. (4.5) in the case of the ^{16}O + ^{208}Pb system at E_{lab}=80 MeV, where nonlocality is very large (See Fig. 1). The solid curve is the resultant imaginary part of the $\ell = 10$ DPP, while the dashed and dotted curves represent contribution from $ImU^N(r,r')$ and $ReU^N(r,r')$ (fictitious) parts, respectively.

4.1.2 Taylor expansion method

Perey and Buck[8] assumed a separable form of a nonlocal potential with a Woods-Saxon type local part, $U^{N,local}$, and a Gaussian type nonlocal part. They defined $\beta\mathbf{s} = \mathbf{r} - \mathbf{r}'$ where β is a nonlocality parameter, expanded U^N and χ^N in Taylor series, and performed an integration over $\mathbf{s}$. By assuming again $\chi^L_\ell = \chi^N_\ell$, and by neglecting the surface effect of the local part, $U^{N,local}$, they could relate U^L to $U^{N,local}$ as

$$U^L(\mathbf{r}) \exp[\frac{m\beta^2}{2\hbar^2}(E - U^L(\mathbf{r})] = U^{N,local}(\mathbf{r}) \tag{6}$$

This method only works well when the nonlocality of the potential has a Gaussian form, otherwise integration is difficult to perform and it cannot be placed into a simple analytic form.

4.1.3 Fourier transformation method

Following the famous Perey-Saxon's local energy approximation[20] to nonlocality through the Fourier transform, Madsen and Osterfeld[21] recently developed a simple Fourier transformation technique for the localization of the imaginary optical potential. They defined coordinates $s = r - r'$ and $\frac{1}{2}(r + r') = r + \frac{1}{2}s$, and again assumed $\chi^L_\ell = \chi^N_\ell$. The Perey-Saxon's local energy approximation is then applied to the radial nonlocal potential as

$$\begin{aligned} U^L_\ell(r)\chi^L_\ell(r) &= \int dr' U^N_\ell(r, r')\chi^N_\ell(r') \\ &\approx \int ds U^N_\ell(r, r - \frac{s}{2})\chi^L_\ell(r - \frac{s}{2}) \\ &\approx 2\pi \mathcal{U}^N_\ell(r, \kappa)\chi^L_\ell(r). \end{aligned} \tag{7}$$

where $\mathcal{U}^N_\ell(r, \kappa)$ is a simple Fourier transformation of $U^N_\ell(r, r - \frac{s}{2})$

$$\mathcal{U}^N_\ell(r, \kappa) = \frac{1}{2\pi}\int_{-\infty}^{\infty} ds U^N_\ell(r, s)e^{-i\kappa s} \tag{8}$$

where κ is chosen equal to the local wave number

$$\kappa = \kappa_\ell = [\frac{2m}{\hbar^2}(E - V(r)) - \frac{\ell(\ell + 1)}{r^2}]^{1/2} \tag{9}$$

for a given ℓ. It should be noted that this approximation induces local momentum (or energy) dependence in the localized potential and in addition there is another energy dependence of the local optical potential due to localization.

4.1.4 Comparisons in the Perey-Buck nonlocal potential

We now compare these three localization methods to the Perey-Buck nonlocal potential,[8] which consists of a Woods-Saxon type local part $U^{N,local}$ and a Gaussian type nonlocal part H as,

$$U^N(\mathbf{r}, \mathbf{r}') = U^{N,local}((\mathbf{r} + \mathbf{r}')/2)H(|\mathbf{r} - \mathbf{r}'|), \tag{10}$$

$$H(|\mathbf{r} - \mathbf{r}'|) = \frac{1}{(\sqrt{\pi}\beta)^3} exp[-(\frac{\mathbf{r} - \mathbf{r}'}{\beta})^2]. \tag{11}$$

The radial part of the nonlocal potential in Eq. (3.7) for this case then becomes

$$U^N_\ell(r, r') = U^{N,local}((r + r')/2)h_\ell(r, r'), \tag{12}$$

and

$$h_\ell(r, r') = \frac{1}{(\sqrt{\pi}\beta)} exp[-(\frac{r^2 + r'^2}{\beta^2})](2i^\ell z j_\ell(-iz)) \tag{13}$$

where $z = \frac{2rr'}{\beta^2}$ and $j_\ell(z)$ is a spherical Bessel function. Fig. 5 displays the imaginary part ($\ell = 0$) of the nonlocal potential of which $U^{N,local}$ has a surface type(derivative of the Woods-Saxon). The calculated real(a) and imaginary(b) parts of the localized DPP from the three methods are shown in Fig. 6. The solid, dashed, and dotted curves denote the results of the TELP method, Taylor expansion method, and Fourier transformation technique, respectively. The potentials look similar to each other as seen in Fig. 6, but generate quite different elastic differential cross sections as described below. The elastic scattering cross sections for the $n + {}^{208}Pb$ at $E_n = 7$ MeV by using potentials obtained from the corresponding methods are displayed in Fig. 7. The *exact* differential cross section from the nonlocal calculation of Sec. 3.2 coincides with the TELP result. The elastic results, except for that of TELP, are unfortunately quite different from the nonlocal one and it becomes even more severe as the nonlocality gets larger. From now on, we will use the TELP method which reproduces the correct elastic scattering cross sections even though it has itself drawbacks as mentioned before.

4.2 Localized W_F and W_D

In Fig. 8, we show the localized $W(r, r')$, $W_F(r, r')$, and $W_D(r, r')$ generated for the ${}^{16}\mathrm{O} + {}^{208}\mathrm{Pb}$ system at E_{lab}=80 MeV as solid, dashed, and dotted curves, respectively. The scale in the figure at greater radial distances than 11 fm is magnified. The construction of the DPP is the same as in Sec. 2.1. The localization was carried out for $\ell = 10$. Since only the imaginary parts of the nonlocal potential are localized, the unphysical parts do not contribute. The localized W is well separated into W_F and W_D parts; the inner part of W coincides with W_F, while the outer part with W_D. A similar separation is also seen for different partial waves. It is worth noting that W_F extends out to about 12 fm, which is definitely outside the Coulomb barrier, supporting the direct reaction approach to fusion[1,4].

4.3 Comparison of a localized DPP with the phenomenological OM potential

We assume that there exists an equivalent local potential to the nonlocal DPP, and then derive this local potential by using the TELP method. This local potential is then compared to a phenomenological optical model potential. Since it is impossible to construct a nonlocal DPP including all the open and closed channels formed by the two colliding nuclei at this stage, we restrict ourself to a limited CC space, perform CC calculations in that space, and treat the CC results as a data set. We now obtain a phenomenological ℓ-independent OM potential by performing χ^2- fitting to CC results. On the other hand, we construct the nonlocal DPP in this limited CC space, and localize it by using the TELP method. The approximated ℓ-independent local potential is then obtained from the ℓ-dependent localized potential as follows[22],

$$U(r) = \frac{\sum_\ell (2\ell+1) T_\ell U_\ell(r)}{\sum_\ell (2\ell+1) T_\ell} \tag{14}$$

where T_ℓ is the transmission coefficient of Eq. (3.19). We then compare the two potentials with each other.

For this purpose, we choose the ${}^{16}\mathrm{O} + {}^{40}\mathrm{Ca}$ system at E_{lab}=60 MeV, of which the CC potential is known[23]. The same CC space is chosen as that of Ref. 23, i.e., coupling of the ground state to the 3.90 MeV 2^+, 3.74 MeV 3^-, and 4.49 MeV 5^- states in ${}^{40}\mathrm{Ca}$. The coupling strengths are also obtained from Ref. 23. In Fig. 9, the solid curve is the resultant localized potential, while the dashed one the phenomenological potential obtained by a χ^2- fitting to the CC results. The dotted curve is the imaginary part of CC potential used in the calculation. Except for values around 8 fm, the two potentials agree nicely. However, we cannot conclude that an equivalent local potential to the nonlocal one always exists, because the TELP method itself has some drawbacks as mentioned before. A better localization procedure should be made for a highly nonlocal potential.

5 Summary

We have studied the dynamic polarization potential due to the coupling to collective states, based on the projection operator formalism of Feshbach. It turns out to be nonlocal and ℓ-dependent. Dispersion relations between the real and imaginary parts were discussed.

We have presented how to calculate the elastic, direct reaction, and fusion cross sections simultaneously with a single DPP. For this purpose, a rapid way to solve the nonlocal Schrödinger equation was developed to obtain the *exact* solution. The separation of the DPP into the direct reaction and fusion parts was then formulated. We showed that such a separation phenomenologically made in a local space explains well the observed data.
In order to justify the phenomenological local optical model potential, localization procedures of the nonlocal DPP were discussed. A few attempts with the trivially equivalent local potential method were made to account for the phenomenological fusion potential which has a large fusion radius. It turns out that the localized fusion potential indeed exists out to a large radial distance, supporting the direct reaction approach to fusion. In a limited coupled-channels space, we constructed both a localized polarization potential and a phenomenological potential which fits the coupled-channels results. We found that these two potentials agree reasonably well with each other. Nevertheless, there is still room to justify phenomenological local optical potential with a dynamic polarization potential. It is too early to give a definite answer whether or not the equivalent local potential to the nonlocal one always exists. A better localization procedure should be made for a highly nonlocal potential. At this time we are not in a position to construct a full dynamic polarization potential which includes all the necessary ingredients.
Most of this work were carried out by a collaboration with Prof. T. Udagawa during the stay at the University of Texas at Austin. I thank Dr. D. Knobles for a careful reading of the manuscript. This work was supported in part by the Ministry of Education, through the Basic Science Institute Program, 1990, and in part by the U. S. Department of Energy.

References

[1] T.Udagawa, B. T. Kim, and T. Tamura, Phys. Rev. **C32** (1985) 124.

[2] G. R. Satchler, M. A. Nagarajan, J. S. Lilley, and I. J. Thompson, Ann. Phys. **178** (1987) 110.

[3] G. R. Satchler, *Direct reaction theories*, (Oxford, London, 1984).

[4] B. T. Kim, in *Proc. of the 1st Sorak symposium on nuclear physics, Sorak, 1988*, ed. D. P. Min, p.235.

[5] B. T. Kim, in *Proc. of the RIKEN symposium on nuclear collective motion and nuclear reaction dynamics, Wako, Japan, 1989.*

[6] H. Feshbach, Ann. Phys. **5** (1958) 357, ibid, **19** (1962) 287.

[7] M. A. Nagarajan, C. Mahaux and G. R. Satchler, Phys. Rev. Lett. **54** (1985) 1136.

[8] F. Perey and B. Buck, Nucl. Phys. **32**(1962) 353.

[9] B. T. Kim and T. Udagawa, Phys. Rev. C **42** (1990) 1147.

[10] R. R. Whitehead, A. Watt, B. J. Cole, and I. Morrison, Adv. Nucl. Phys. **9**(1977) 123.

[11] G. R. Satchler, Phys. Rev. C **32** (1985) 2203.

[12] B. T. Kim, M. Naito, and T. Udagawa, Phys. Lett. **237B** (1990) 19.

[13] M. J. Rhoades-Brown and M. Prakash, Phys. Rev. Lett. **53** (1984) 333.

[14] B. T. Kim, H. C. Kim and K. E. Park, Phys. Rev. C **37**, (1988) 998.

[15] C. Mahaux, H. Ngo and G. R. Satchler, Nucl. Phys. **A449** (1986) 354; Nucl. Phys. **A456** (1986) 134.; M. A. Nagarajan, C. Mahaux and G. R. Satchler, Phys. Rev. Lett. **54** (1985) 1136.

[16] G. R. Satchler and W. G. Love, Phys. Rep. **55** (1979) 183.

[17] F. Videvaek *et al.*, Phys. Rev. C **15** (1977) 954.

[18] E. Valgaris, L. Gradzins, S. G. Steadman and R. Ledoux, Phys. Rev. C **33** (1986) 2017.

[19] M. A. Franey and P. J. Ellis, Phys. Rev. C **23** (1981) 787.

[20] F. G. Perey and D. S. Saxon, Phys. Lett. **10** (1964) 107.

[21] V. A. Madsen and F. Osterfeld, Phys. Rev. C **39** (1989) 1215.

[22] I. J. Thompson, M. A. Nagarajan, J. S. Lilley and M. J. Smithson, Nucl. Phys. A **505** (1989) 84.

[23] K. I. Kubo and P. E. Hodgson, Nucl. Phys. **A366** (1981) 320.

Chap. 7
Dynamic Polarization Potential – figures

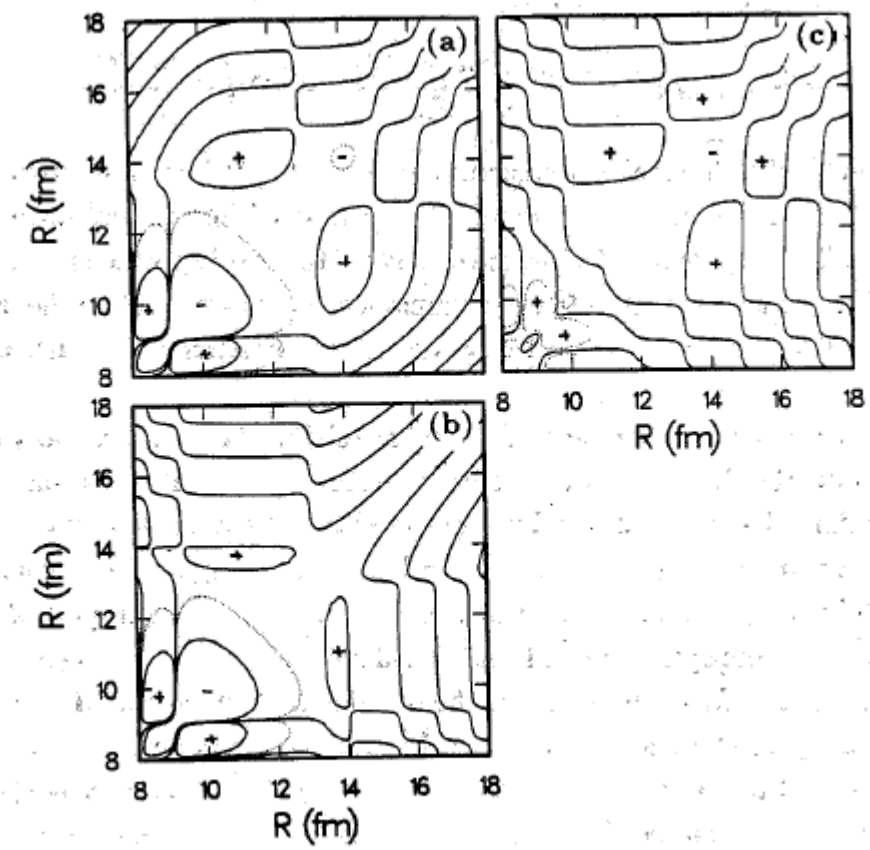

Figure 1: The imaginary part(a) of $\ell = 10$ DPP for the $O+Pb$ system at E_{lab}=80 MeV. The imaginary part is further decomposed into fusion(b) and direct reaction(c) parts.

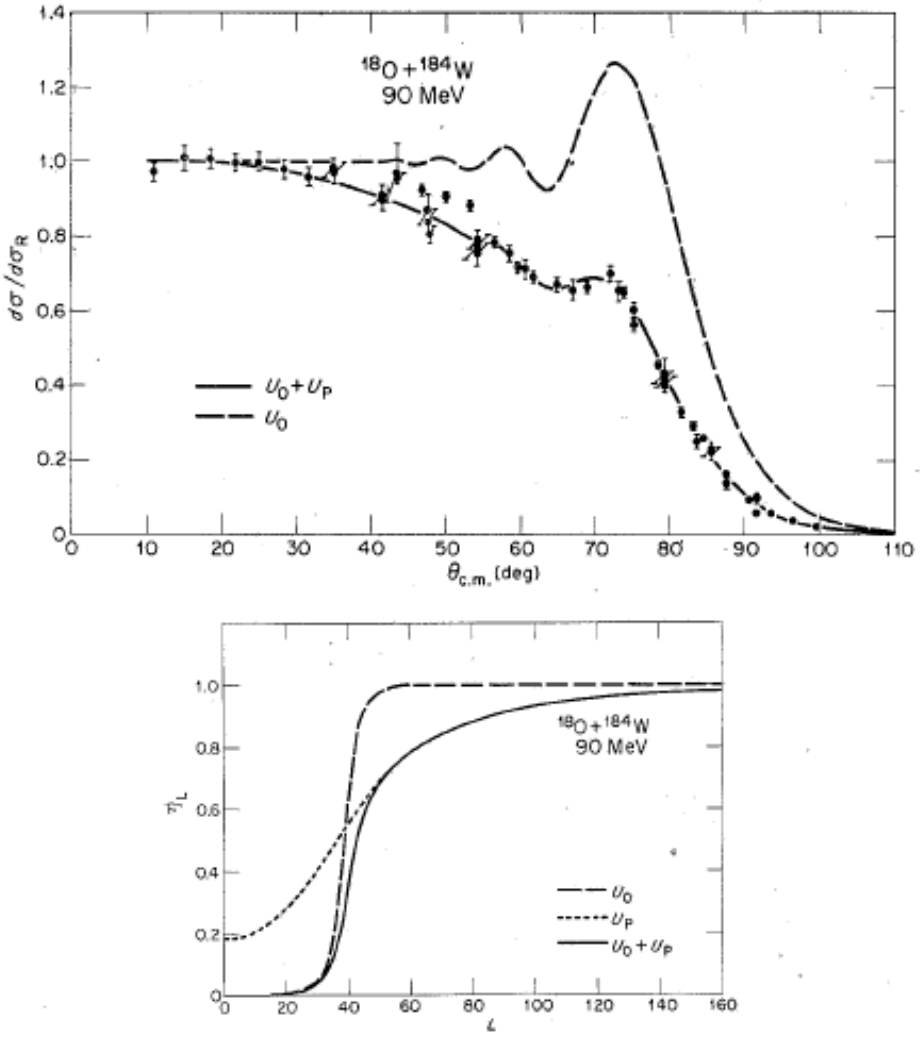

FIG. 12.10. Effects of the long-ranged absorption due to Coulomb excitation (a) on the cross sections for elastic scattering of $^{18}O + ^{184}W$, and (b) on the reflection coefficients η_L. Here U_0 is a conventional (complex) Woods–Saxon potential while U_p is the (imaginary) dynamic polarization potential (12.64) that represents the effects of the Coulomb excitation (primarily of the first 2^+ state in ^{184}W). (From Love et al. 1977.)

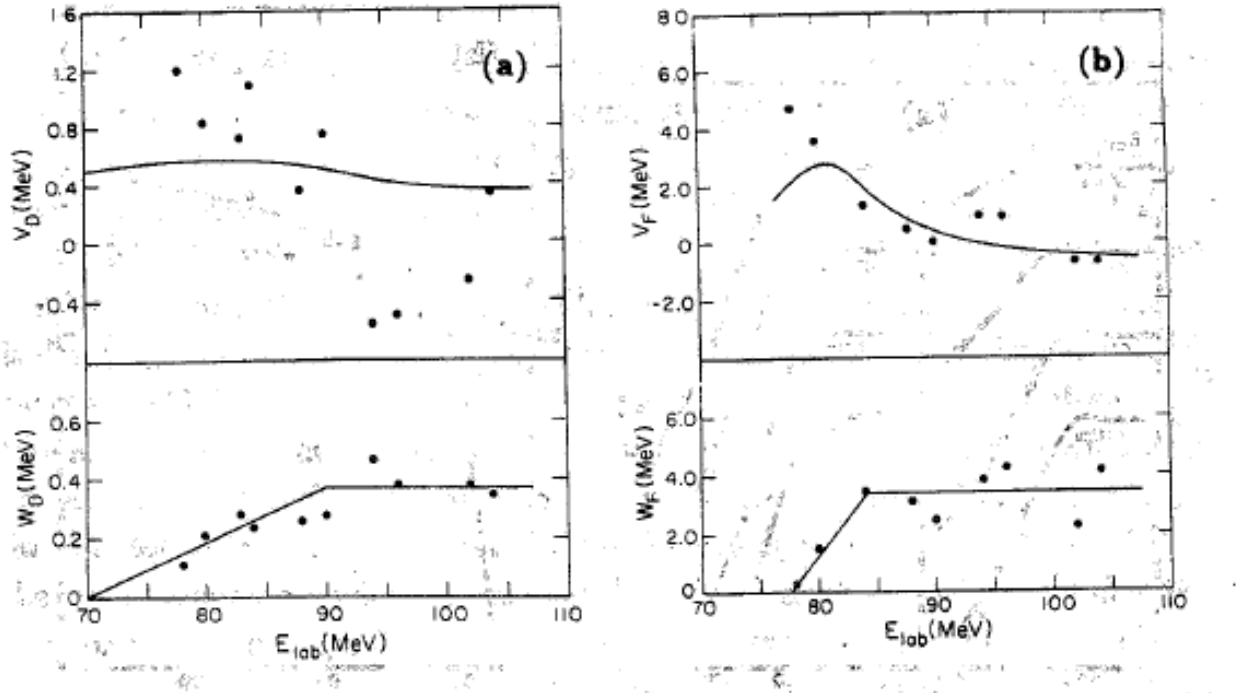

Figure 2: Strength parameters $V_D(E)$ and $W_D(E)$ of the direct reaction potential(a) as functions of E. The dots are those extracted from the χ^2-analyses, while the full lines drawn for W_D and $V_D(E)$ are the predictions of Eq. (3.31) and Eq. (3.30) using (3.31), respectively. (b) is the same as (a) but for the fusion potential. The full lines drawn for W_F and $V_F(E)$ are the predictions of Eq. (3.32) and Eq. (3.30) using (3.32), respectively.

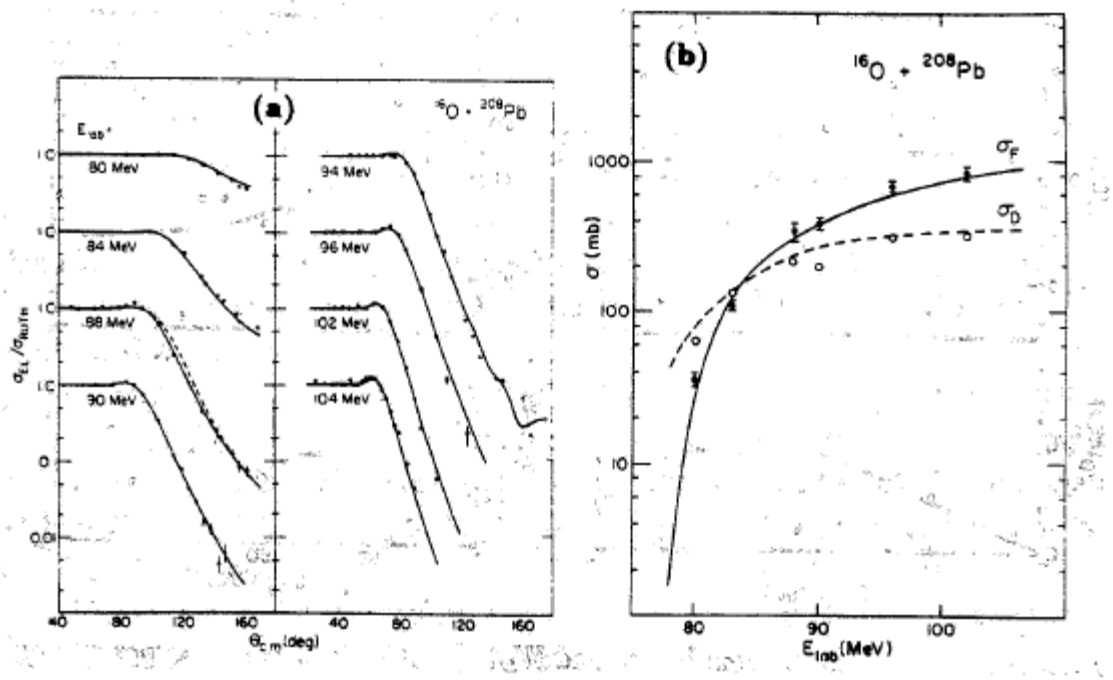

Figure 3: Comparison of the calculated ratio R of the elastic scattering cross sections to Rutherford cross sections(a), and the calculated direct reaction, fusion, and total reaction cross sections(b) using our final optical potential for the $O+Pb$ system, with the experimental data. The broken line shown for E_{lab}=88 MeV is R calculated by neglecting $V_D(r)$. The data are taken from Refs. 17 and 18.

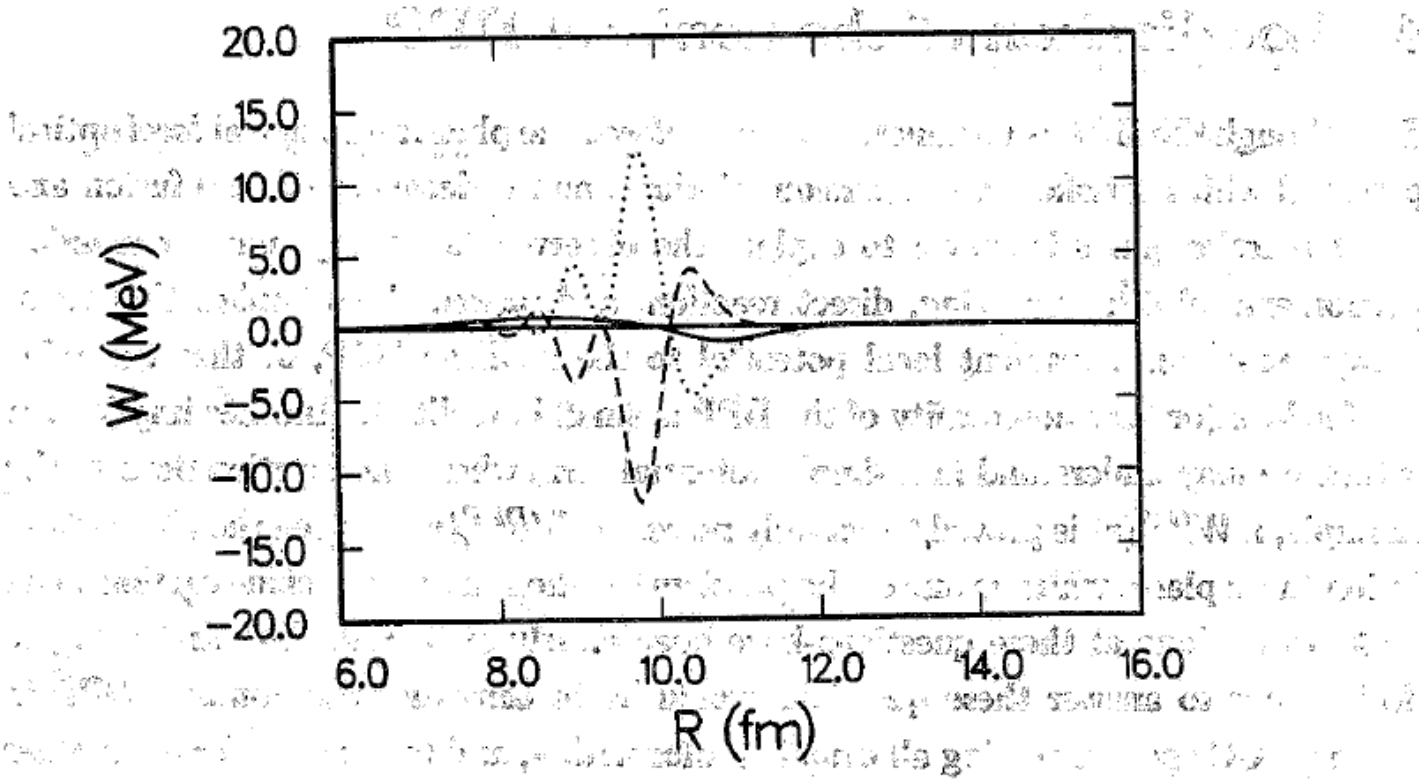

Figure 4: Imaginary part(solid) of the potential obtained from a TELP localization method. The dashed curve denotes contribution from the imaginary part of $U^N(r, r')$, while the dotted one from the real part.

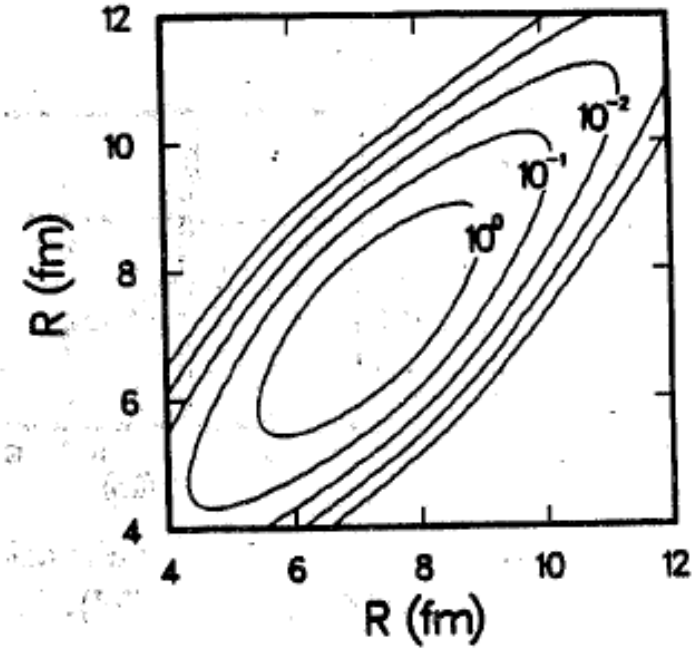

Figure 5: Imaginary part of Perey-Buck nonlocal potential for the n + Pb system at $E_n = 7$ MeV.

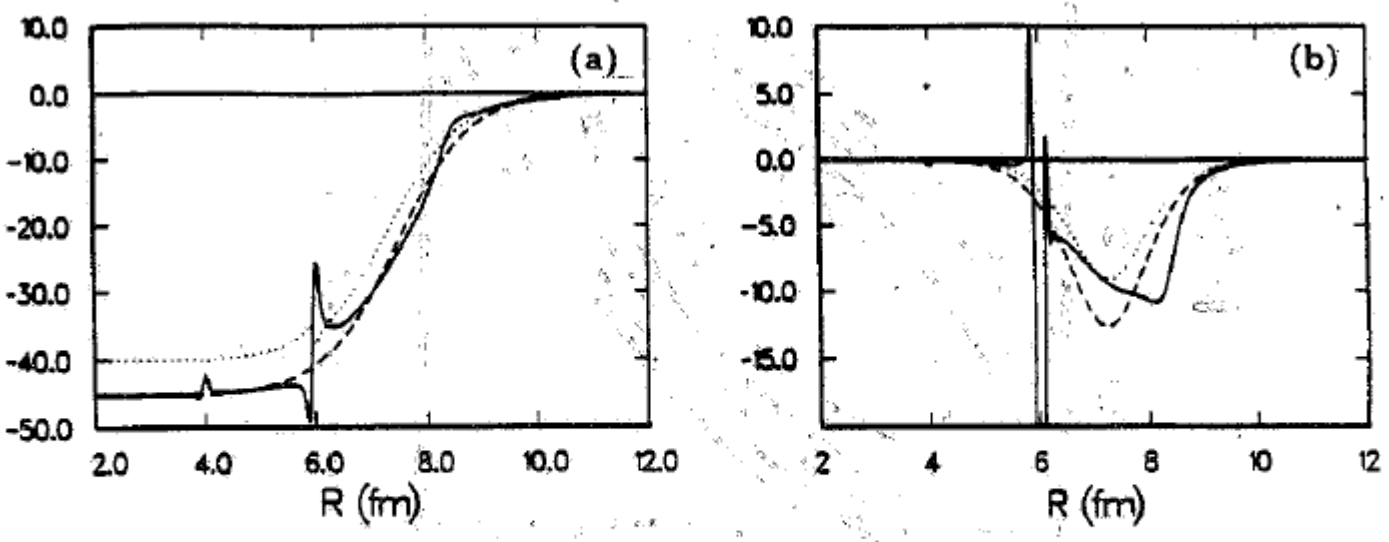

Figure 6: Localized real(a) and imaginary(b) parts of Perey-Buck nonlocal potential for the $n + Pb$ system at $E_n = 7$ MeV obtained from TELP (solid), Taylor expansion (dashed) and Fourier transformation (dotted) methods.

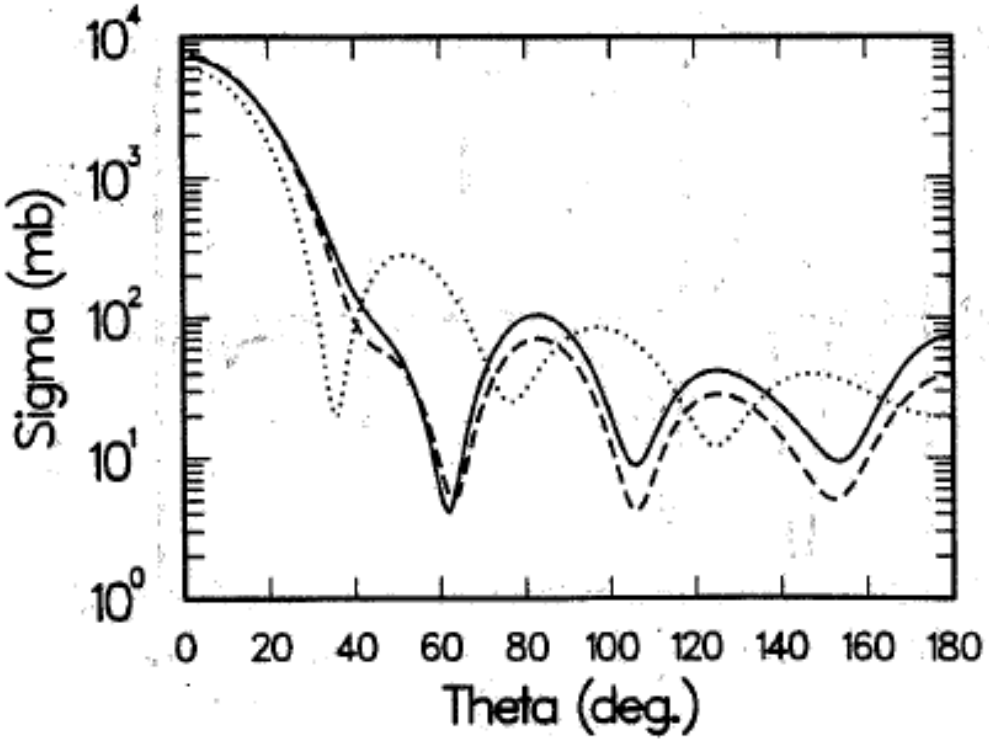

Figure 7: Elastic differential cross sections for the $n + Pb$ system at $E_n = 7$ MeV by using potentials obtained from TELP (solid), Taylor expansion (dashed) and Fourier transformation (dotted) methods. The exact cross section coincides with the solid curve.

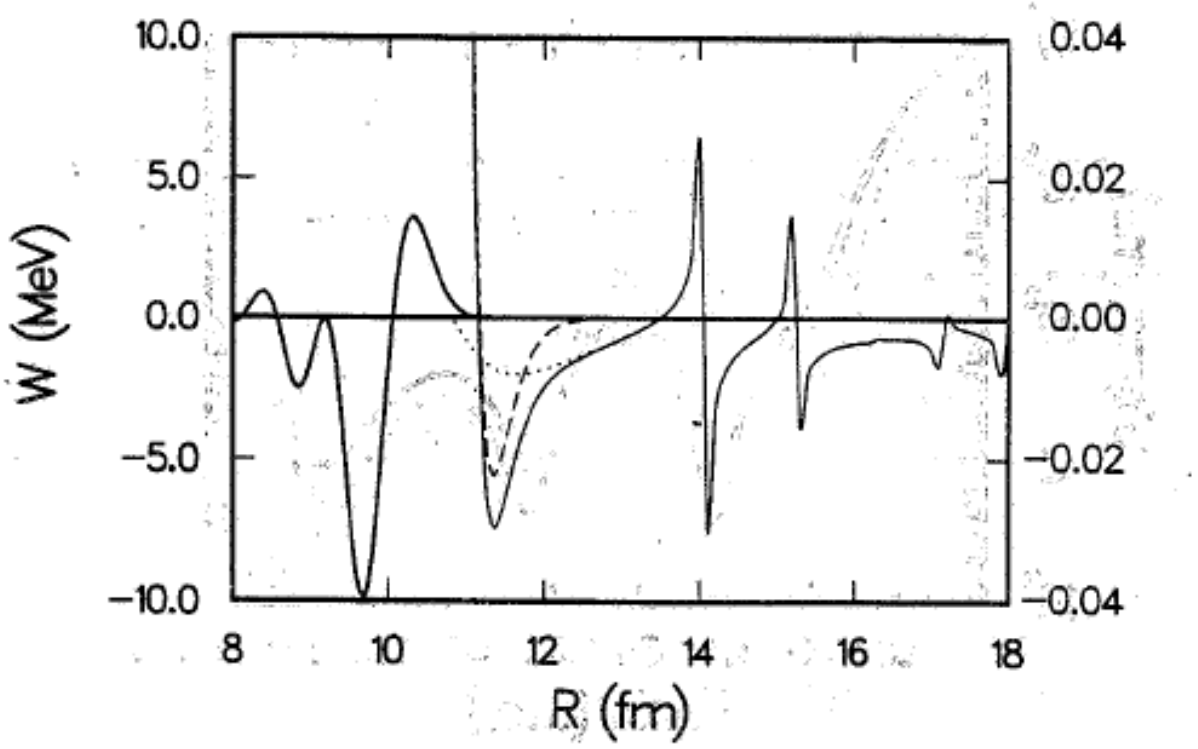

Figure 8: Separation of a localized W(solid) into W_F(dashed) and W_D(dotted).

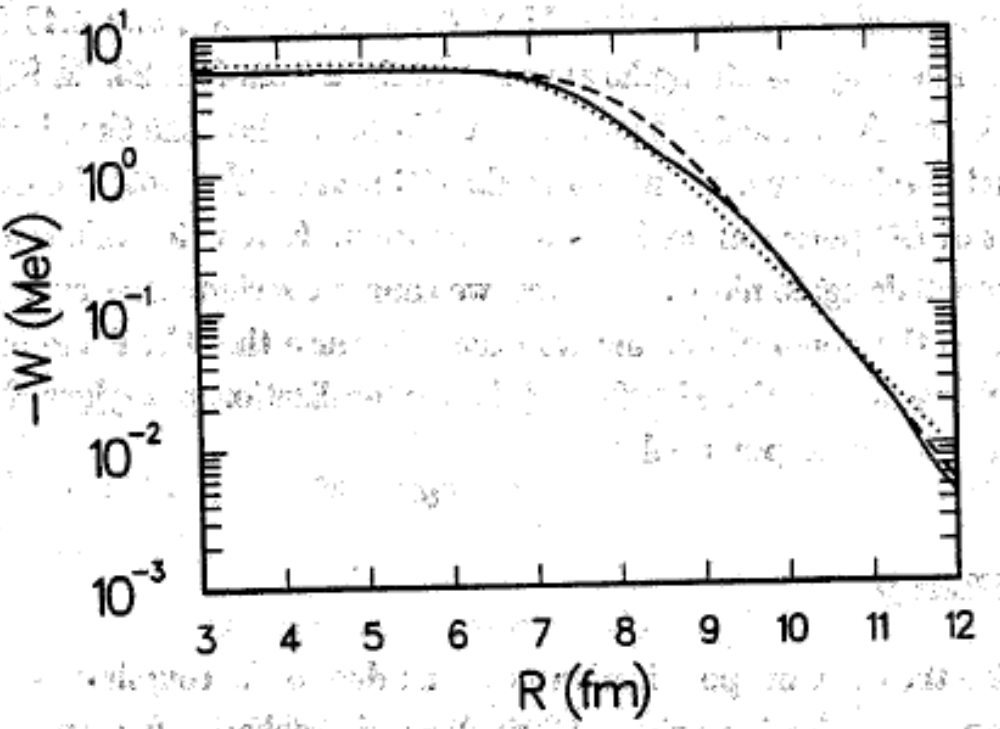

Figure 9: Comparison of $W^{localizedDPP}$(solid) with W^{OM}(dashed) for the $O + Ca$ system at E_{lab}=60 MeV. The dotted curve is the imaginary part of CC potential. The coupling scheme is mentioned in the text.

Chap. 7
Dynamic Polarization Potential – figures

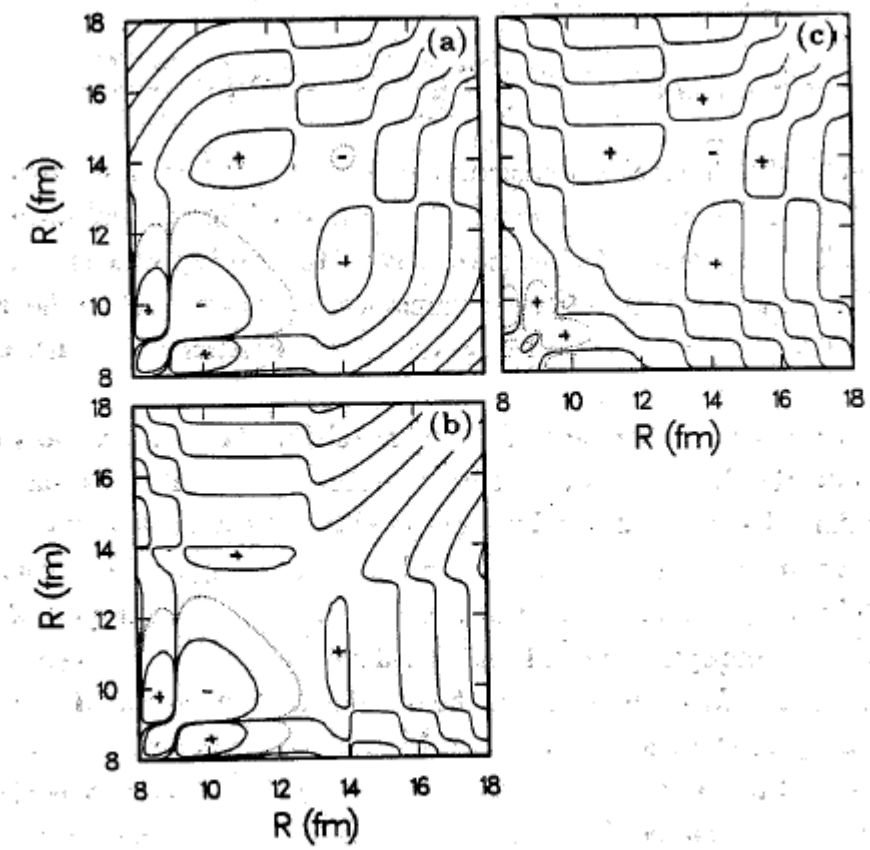

Figure 1: The imaginary part(a) of $\ell = 10$ DPP for the $O+Pb$ system at E_{lab}=80 MeV. The imaginary part is further decomposed into fusion(b) and direct reaction(c) parts.

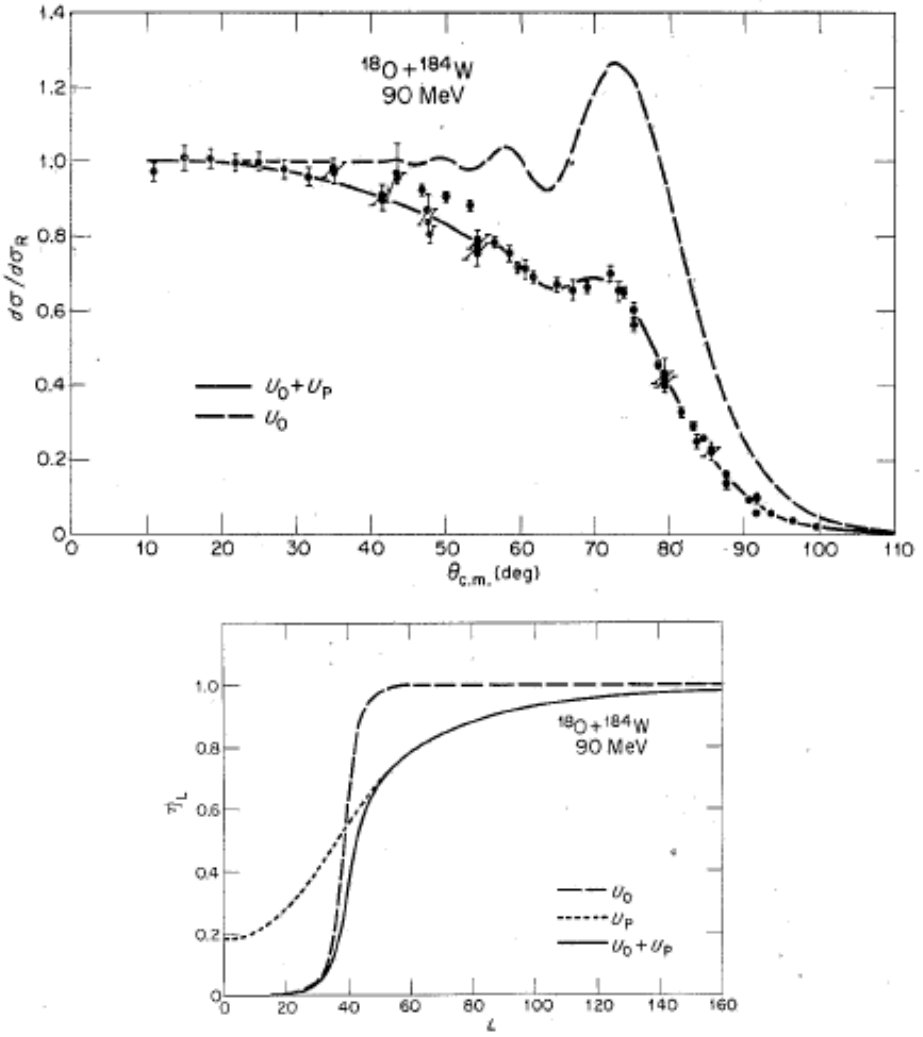

FIG. 12.10. Effects of the long-ranged absorption due to Coulomb excitation (a) on the cross sections for elastic scattering of $^{18}O + ^{184}W$, and (b) on the reflection coefficients η_L. Here U_0 is a conventional (complex) Woods–Saxon potential while U_p is the (imaginary) dynamic polarization potential (12.64) that represents the effects of the Coulomb excitation (primarily of the first 2^+ state in ^{184}W). (From Love et al. 1977.)

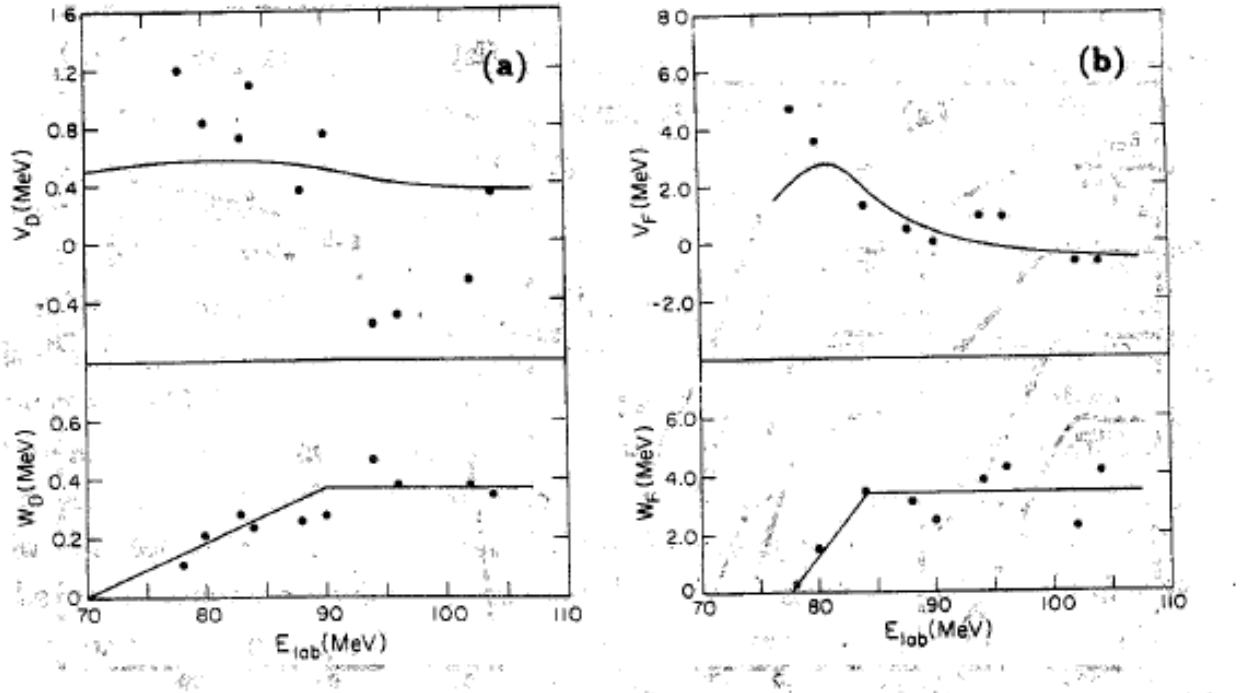

Figure 2: Strength parameters $V_D(E)$ and $W_D(E)$ of the direct reaction potential(a) as functions of E. The dots are those extracted from the χ^2-analyses, while the full lines drawn for W_D and $V_D(E)$ are the predictions of Eq. (3.31) and Eq. (3.30) using (3.31), respectively. (b) is the same as (a) but for the fusion potential. The full lines drawn for W_F and $V_F(E)$ are the predictions of Eq. (3.32) and Eq. (3.30) using (3.32), respectively.

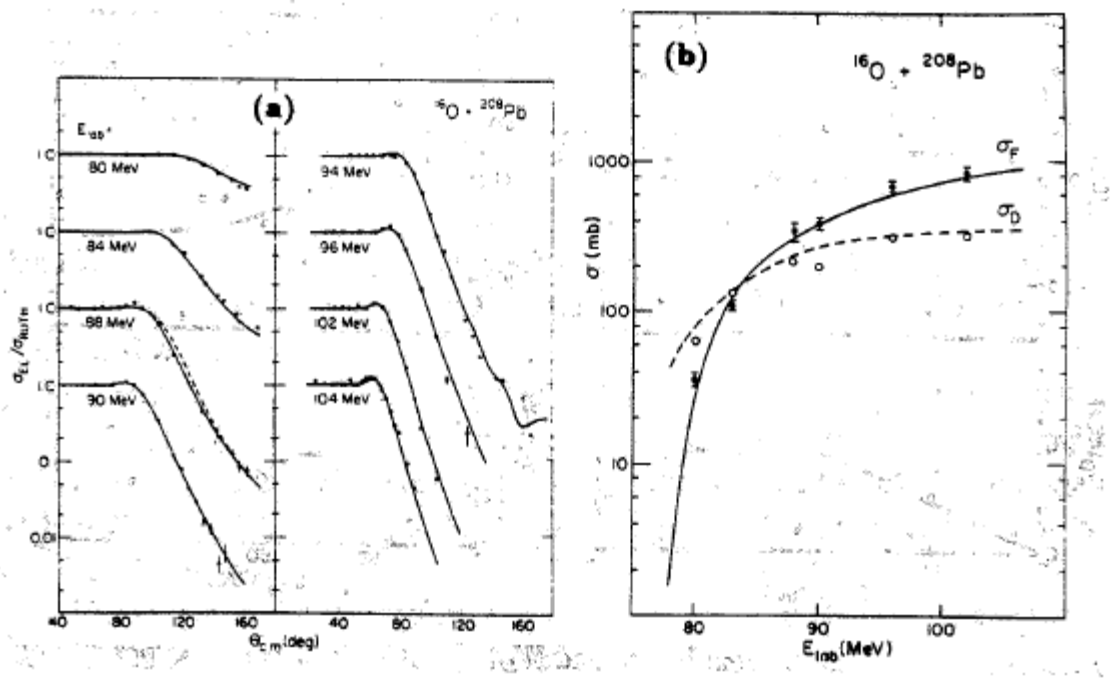

Figure 3: Comparison of the calculated ratio R of the elastic scattering cross sections to Rutherford cross sections(a), and the calculated direct reaction, fusion, and total reaction cross sections(b) using our final optical potential for the $O+Pb$ system, with the experimental data. The broken line shown for E_{lab}=88 MeV is R calculated by neglecting $V_D(r)$. The data are taken from Refs. 17 and 18.

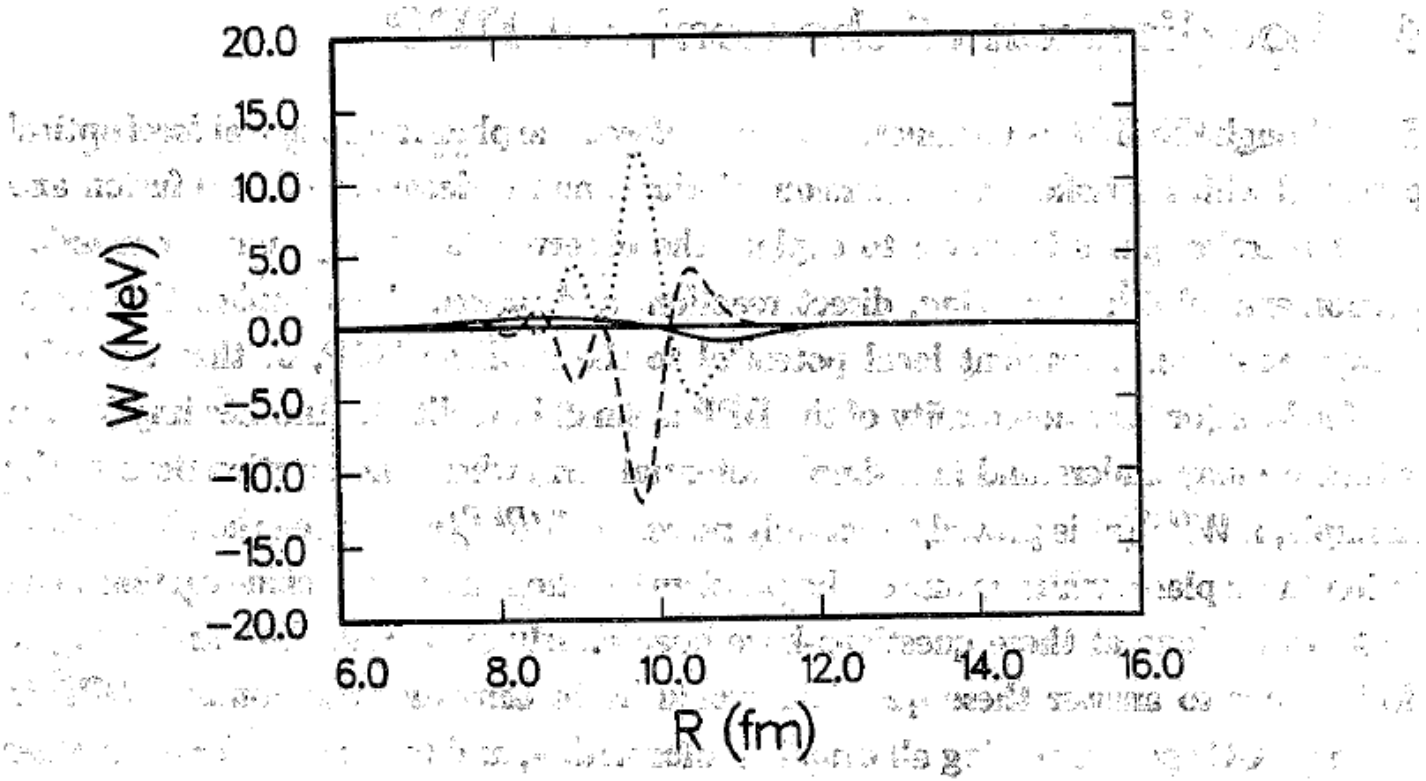

Figure 4: Imaginary part(solid) of the potential obtained from a TELP localization method. The dashed curve denotes contribution from the imaginary part of $U^N(r, r')$, while the dotted one from the real part.

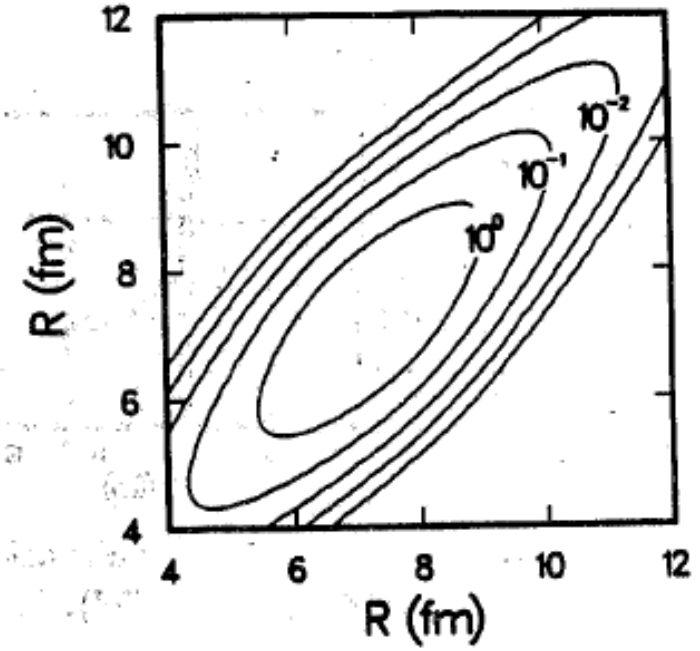

Figure 5: Imaginary part of Perey-Buck nonlocal potential for the n + Pb system at $E_n = 7$ MeV.

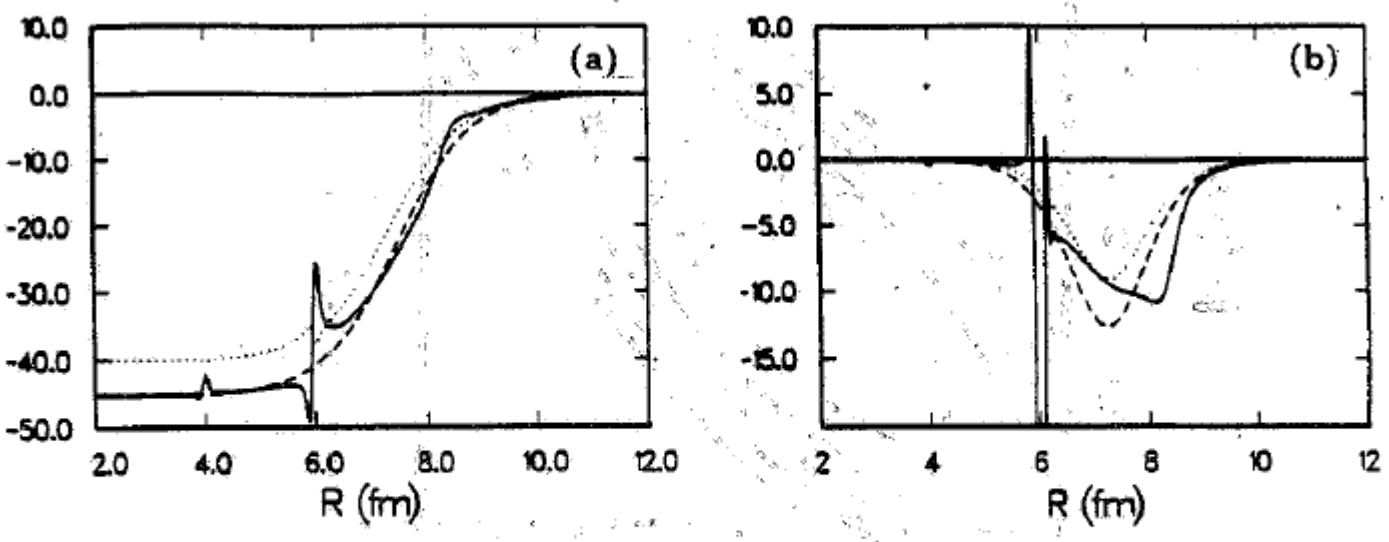

Figure 6: Localized real(a) and imaginary(b) parts of Perey-Buck nonlocal potential for the $n + Pb$ system at $E_n = 7$ MeV obtained from TELP (solid), Taylor expansion (dashed) and Fourier transformation (dotted) methods.

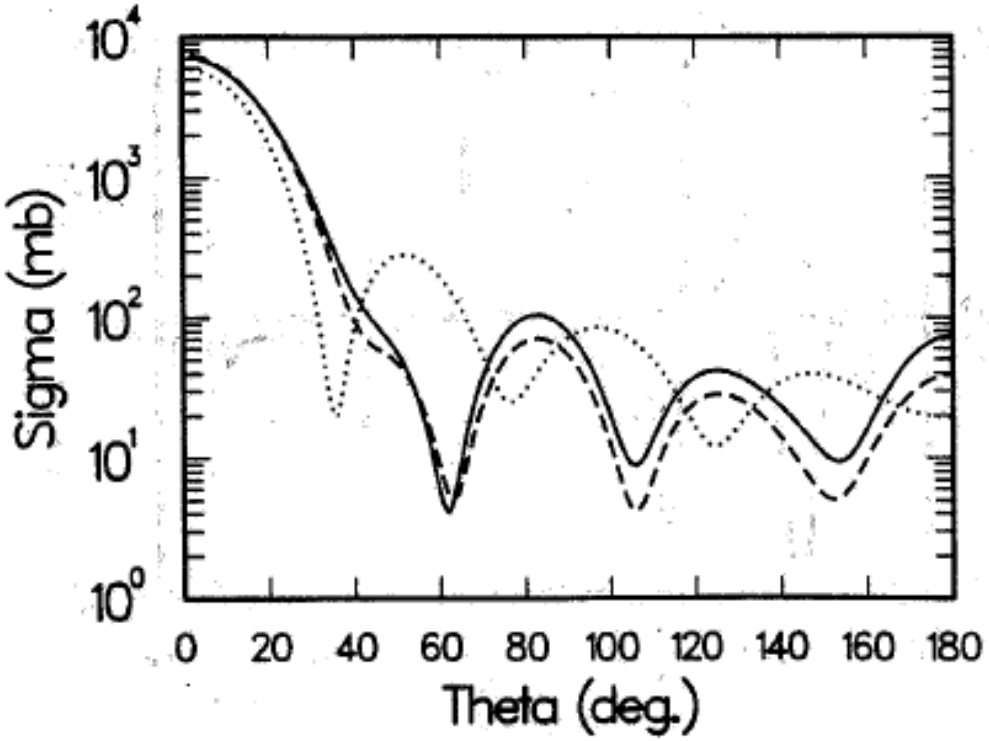

Figure 7: Elastic differential cross sections for the $n + Pb$ system at $E_n = 7$ MeV by using potentials obtained from TELP (solid), Taylor expansion (dashed) and Fourier transformation (dotted) methods. The exact cross section coincides with the solid curve.

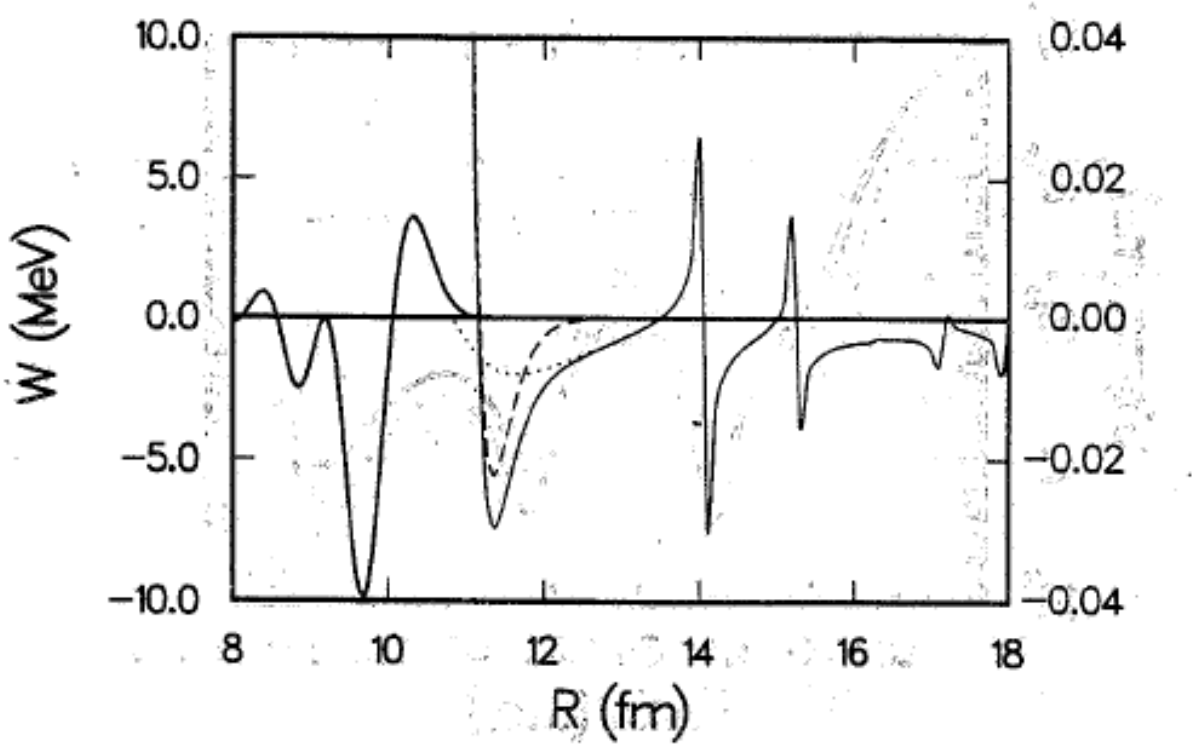

Figure 8: Separation of a localized W(solid) into W_F(dashed) and W_D(dotted).

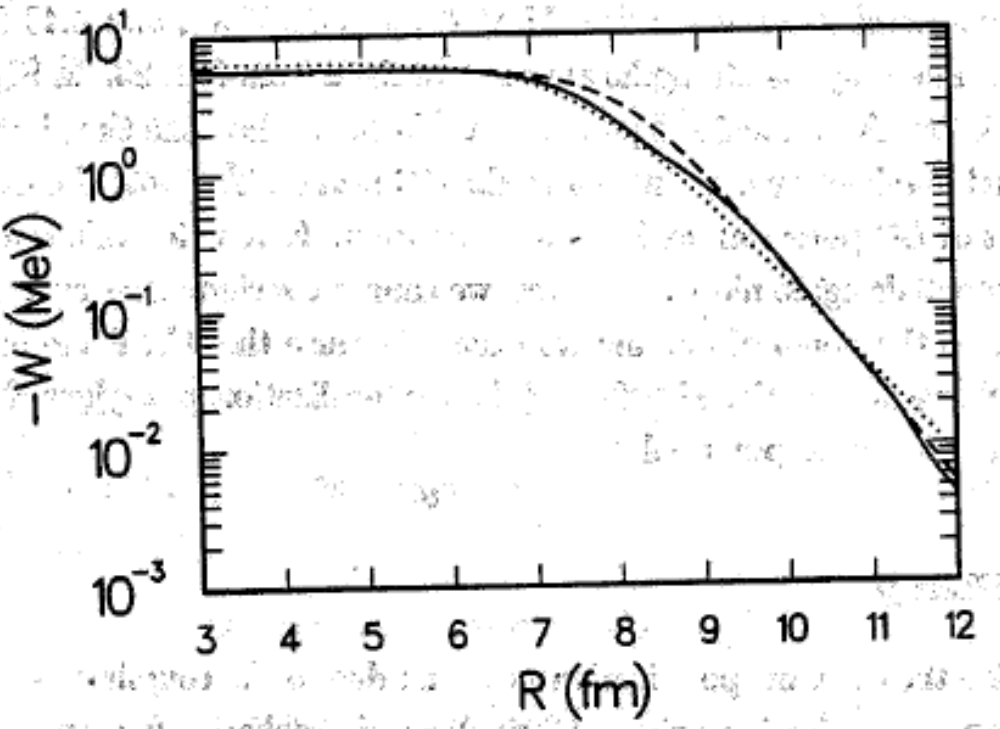

Figure 9: Comparison of $W^{localizedDPP}$(solid) with W^{OM}(dashed) for the $O + Ca$ system at E_{lab}=60 MeV. The dotted curve is the imaginary part of CC potential. The coupling scheme is mentioned in the text.